

# 1 Role of chamber replenishment in the formation of the Merensky 2 Reef and its footwall anorthosite

3 William D. Smith<sup>1</sup>, Hadrien Henry<sup>2</sup>, Jussi S. Heinonen<sup>3,4</sup>, Wolfgang D. Maier<sup>5</sup>, Duncan D. Muir<sup>5</sup>,  
4 Sarah-Jane Barnes<sup>6</sup>, and Jens Ø. Andersen<sup>7</sup>

5  
6 <sup>1</sup>CSIRO Mineral Resources, 26 Dick Perry Avenue, Kensington, Perth, WA 6151, Australia

7 <sup>2</sup>Géosciences Environment Toulouse, Université de Toulouse III Paul Sabatier, 14 Avenue E. Belin,  
8 31400 Toulouse, France

9 <sup>3</sup>Department of Geosciences and Geography, University of Helsinki, P.O. Box 64, 00014, Helsinki,  
10 Finland

11 <sup>4</sup>Geology and Mineralogy, Åbo Akademi University, Akademigatan 1, 20500 Åbo, Finland

12 <sup>5</sup>School of Earth & Environmental Sciences, Cardiff University, United Kingdom, CF10 3AT

13 <sup>6</sup>Sciences de la Terre, Université du Québec à Chicoutimi, 555 Boulevard de l'Université, Quebec G7H  
14 2B1, Canada

15 <sup>7</sup>Camborne School of Mines, University of Exeter, Penryn, United Kingdom, TR10 9EZ

16  
17 \*Corresponding author: [will.smith@csiro.au](mailto:will.smith@csiro.au)

## 18 19 Abstract

20 The Merensky Reef of the Bushveld Complex represents a magmatic unconformity that some  
21 researchers attribute to chamber replenishment by relatively primitive magma. It is  
22 propounded that cumulate rocks in this chamber reacted with replenishing melt, as part of the  
23 process that ultimately produced chromitite stringers and reef-style platinum-group element

24  
25 © The Author(s) 2025. Published by Oxford University Press. This is an Open Access article distributed  
26 under the terms of the Creative Commons Attribution License  
27 <https://creativecommons.org/licenses/by/4.0/>, which permits unrestricted reuse, distribution, and  
28 reproduction in any medium, provided the original work is properly cited.

29 mineralization. This study investigates as to whether chamber replenishment contributed to  
30 the formation of the Merensky Reef and its underlying anorthosite at the Rustenburg Platinum  
31 Mine in the western lobe of the Bushveld Complex.

32  
33 At this location, the Merensky Reef is a coarse-grained pyroxenite bracketed by millimeter-  
34 scale chromitite stringers. This sequence is underlain by a centimeter-scale anorthosite which  
35 in turn is underlain by leuconorite. The leuconorite comprises normally zoned cumulus  
36 orthopyroxene with poikilitic rims ( $Mg_{80-79}$ ) and cumulus plagioclase ( $An_{80-58}$ ), where the latter  
37 defines a magmatic fabric indicative of gravitational settling of tabular crystals in a quiescent  
38 melt. The contact between leuconorite and anorthosite is marked by an increased abundance  
39 of late-stage accessory minerals, and the composition of poikilitic orthopyroxene at this  
40 horizon is consistent with trapped liquid shift. Plagioclase crystals in the anorthosite are  
41 variably zoned ( $An_{79-64}$ ) and record a magmatic fabric that strengthens with proximity to the  
42 reef. This unit is traversed by sinuous networks of sulfides, pyroxenes, quartz, and very fine-  
43 grained chromite that terminate at the contact with the leuconorite. The lower chromitite hosts  
44 both amoeboidal and blocky chromite crystals that are enclosed by complexly zoned  
45 plagioclase oikocrysts in the lower two-thirds and by orthopyroxene oikocrysts in the upper  
46 third. The upper chromitite hosts only blocky crystals, similar to those in the upper portion of  
47 the lower chromitite. Microtextural characteristics of the amoeboidal crystals coupled with their  
48 propensity to host polymineralic inclusions, suggests that these were initially skeletal crystals  
49 that subsequently underwent dissolution-reprecipitation. There is no discernible chemical  
50 difference between amoeboidal and blocky crystals; however, accessory mineralogy and  
51 chromite chemistry imply that the upper portion of the lower chromitite and the upper chromitite  
52 experienced post-cumulus re-equilibration with evolved intercumulus silicate melt.

53 Our observations are consistent with the anorthosite being a restite of partially molten  
54 leuconoritic cumulates. This theory is supported by thermodynamic modelling that  
55 demonstrates that under certain conditions, replenishing melts can reconstitute noritic  
56 cumulates to anorthosite, troctolite, or feldspathic orthopyroxenite restites. The porosity

57 generated during this process was exploited by downward percolating sulfide melt that  
58 displaced a proportionate amount of intercumulus silicate melt upward to the level of the  
59 nascent reef. Initially, these partial melts were likely relatively volatile-rich, triggering Cr-  
60 supersaturation at the cumulate-melt interface, and later became Cr-bearing with the  
61 consumption of poikilitic orthopyroxene and very fine-grained chromite.

62

63 **Keywords:** Merensky Reef, Bushveld Complex, Element Mapping, Mineral Chemistry, EBSD,  
64 Magma Chamber Simulator

ORIGINAL UNEDITED MANUSCRIPT

## 65 1. INTRODUCTION

66 The ~ 2.056 Ga Bushveld Complex (Fig. 1) is the world's largest known layered mafic-  
67 ultramafic intrusion and host to the three most important platinum-group element (PGE)  
68 deposits, namely the UG2 chromitite, Platreef, and Merensky Reef (Eales and Cawthorn 1996;  
69 Maier *et al.* 2013; Cawthorn 2015; Kinnaird and McDonald 2018; Scoates *et al.* 2021; Smith  
70 and Maier 2021). The Merensky Reef can be traced across the extent of the Bushveld  
71 Complex, displaying remarkable uniformity in thickness and lithology (Vermaak 1976; Leeb  
72 du Toit 1986, Viljoen and Hieber 1986, Viljoen *et al.* 1986; Viljoen 1999;; Roberts *et al.* 2007;  
73 Naldrett *et al.* 2009; Latypov *et al.* 2015; Grobler *et al.* 2019). It occurs within the *Upper Critical*  
74 *Zone*, which is characterized by interlayered units of chromitite, pyroxenite, norite, and  
75 anorthosite (Eales *et al.* 1988; Roberts *et al.* 2007). Since its discovery in 1924, the Merensky  
76 Reef has been the focus in research on the formation of stratiform horizons enriched in  
77 precious metals in layered mafic-ultramafic intrusions. Despite a century of investigations, the  
78 petrogenesis of such horizons remains controversial.

79 In general, the Merensky Reef consists of a cm- to m-scale, coarse-grained to pegmatoidal  
80 pyroxenite (*i.e.*, *central pyroxenite*) that is bracketed by mm-scale chromitite layers (*i.e.*, the  
81 lower and upper chromitites) and overlain by several metres of medium-grained pyroxenite,  
82 known as the *hanging-wall pyroxenite* (Viljoen *et al.* 1986; Viljoen 1999; Barnes and Maier  
83 2002; Arndt *et al.* 2005; Naldrett *et al.* 2009; Smith *et al.* 2021). In the western lobe of the  
84 Bushveld Complex, this sequence is typically underlain by leuconorite, anorthosite, and  
85 subordinate troctolite, whereas, in the eastern lobe, it is usually underlain by pyroxenite (Eales  
86 and Cawthorn 1996; Barnes and Maier 2002; Roberts *et al.* 2007; Mitchell and Scoon 2007;  
87 Scoon and Costin 2018; Mitchell *et al.* 2019). Stratiform reef-style PGE mineralization  
88 manifests as PGE-rich disseminated sulfides and platinum-group minerals that are  
89 concentrated in the chromitites and central pyroxenite as well in the immediate footwall rocks  
90 (Viljoen and Hieber 1986; Barnes and Maier 2002; Mitchell and Scoon 2007; Naldrett *et al.*  
91 2009; Mitchell *et al.* 2019; Smith *et al.* 2021; Barnes *et al.* 2022).

92 Several studies have concluded that the Merensky Reef directly overlies a regional  
93 unconformity and is related to a new injection of relatively primitive melt that erodes the  
94 resident cumulate pile (Irvine *et al.* 1983; Campbell 1986; Eales *et al.* 1988; Viljoen 1999;  
95 Viring and Cowell 1999; Roberts *et al.* 2007; Latypov *et al.* 2022). Some researchers have  
96 ascribed the formation of anorthosite and troctolite that underlies the Merensky Reef and  
97 various chromitites to the reconstitution of resident noritic cumulates during reaction with  
98 replenishing melt(s) (Eales *et al.* 1988; Viring and Cowell 1999; Roberts *et al.* 2007; Latypov  
99 *et al.* 2015; Maier and Barnes 2024). It has remained unclear as to whether such a process  
100 can explain the diversity of the Merensky footwall assemblages and contribute to the formation  
101 of stratiform PGE-bearing chromitites. In the present study, we use energy dispersive  
102 spectroscopy (EDS) element mapping, electron backscatter diffraction (EBSD), and mineral  
103 chemistry to characterize the floor rocks of so-called 'normal' Merensky Reef in the western  
104 lobe of the Bushveld Complex. These data are combined with thermodynamic simulations of  
105 footwall reconstitution using the Magma Chamber Simulator (Bohrson *et al.* 2014; 2020). It is  
106 argued that the footwall anorthosite, and indeed other footwall lithologies, form during the  
107 interaction between replenishing silicate melts and resident noritic cumulates.

108

## 109 **2. GEOLOGICAL BACKGROUND**

110 The Bushveld Complex in southern Africa has been described in numerous publications  
111 (Wager and Brown 1968; Eales and Cawthorn 1996; Maier *et al.* 2013; Cawthorn 2015;  
112 Kinnaird and McDonald 2018). The mafic-ultramafic layered rocks are grouped into the  
113 *Rustenburg Layered Suite*, which constitutes a ~ 6-8 km package of cumulate rocks that host  
114 most of the world's PGE and Cr resources as well as significant Ni and Cu resources  
115 (Cawthorn 2015; Mudd *et al.* 2018). The *Rustenburg Layered Suite* is divided into five  
116 stratigraphic units, including the Marginal, Lower, Critical, Main, and Upper Zones (Fig. 1A-B).  
117 The majority of PGE, Cr, and V mineralization is present in the Critical Zone, which is  
118 commonly subdivided into a Lower Critical Zone consisting predominantly of orthopyroxenite

119 with subordinate harzburgite and chromitite and an Upper Critical Zone consisting of  
120 interlayered norite, anorthosite, chromitite, and (ortho)pyroxenite (Cameron 1982).

121 The Merensky Reef occurs at the base of the so-called *Merensky Cyclic Unit* in the Upper  
122 Critical Zone (Fig. 1B). Although seemingly conformable at several localities, the basal contact  
123 of the Merensky Reef sequence may truncate several meters of underlying cumulates,  
124 suggesting that it shares a broadly unconformable contact with its footwall (Vermaak 1976;  
125 Viljoen and Hieber 1986; Viljoen 1999; Viring and Cowell 1999; Barnes and Maier 2002;  
126 Roberts *et al.* 2007; Mitchell and Scoon 2007; Latypov *et al.* 2015; Mitchell *et al.* 2019). The  
127 presence of a magmatic unconformity is supported by the occurrence of elliptical structures  
128 (plan view) that transgress the floor rocks at a variety of scales (*dimples, potholes, and*  
129 *excursions*; Ballhaus 1988; Carr *et al.* 1999; Viring and Cowell 1999; Smith and Basson 2006).  
130 At localities where potholes and undercuttings are present, the Merensky Reef may be  
131 referred to as '*Potholed*' reef (Buntin *et al.* 1985; Ballhaus 1988; Viljoen 1999; Carr *et al.* 1999;  
132 Roberts *et al.* 2007; Latypov *et al.* 2015, 2017). In the western lobe, regional variation in the  
133 nature of the Merensky Reef led to its division into Swartklip and Rustenburg (*cf.* Kroondal  
134 facies of Wagner 1929) facies to the north and south of the Pilanesberg Complex, respectively  
135 (Wagner 1929; Viljoen 1999). In Swartklip facies, the stratigraphic thickness between the  
136 Merensky Reef and UG2 is markedly attenuated and comprises a far greater relative  
137 proportion of olivine-bearing lithologies as well as a PGE-bearing Psuedo Reef package  
138 (Viljoen 1999; Mitchell *et al.* 2019). At Northam (Swartklip facies), the Merensky Reef has  
139 been subdivided into *normal* and *potholed* reef, the latter being underlain by olivine norite and  
140 troctolite (Smith *et al.* 2004; Roberts *et al.* 2007). The Merensky Reef in the Rustenburg facies  
141 is also subdivided into four subfacies; three of which are narrow, pegmatoidal Merensky Reef  
142 overlying anorthosite that display variations in lithological thickness and the degree of  
143 potholing, and the fourth is named non-pegmatoidal wide reef subfacies (Viljoen 1999). Within  
144 the three narrow pegmatoidal Merensky Reef subfacies occurs a *normal* narrow (< 20) reef

145 overlying anorthosite, referred to as *thin reef facies* in Wilson (1999). This is the subject of the  
146 present contribution.

147 In the Rustenburg facies, *normal* Merensky Reef refers to the regionally traceable and planar  
148 portions of the reef stratigraphy that still unconformably overly the footwall lithologies but that  
149 record relative uniformity in thickness and nature. In general, apparently conformable  
150 relationships persist at sites of consolidated melanocratic floor rocks, whereas unconformable  
151 relationships predominantly occur at sites of leucocratic floor rocks (Viring and Cowell 1999).  
152 In the western lobe, leuconorite and anorthosite are the lithologies that most often underlie the  
153 Merensky Reef (Leeb du Toit 1986, Viljoen and Hieber 1986; Maier and Eales 1997). An mm-  
154 to dm-scale layer of anorthosite often separates the leuconorite from the lower chromitite, and  
155 a  $\mu\text{m}$ - to mm-scale layer of “pure” anorthosite (known as the “bleached zone”) directly  
156 underlies the lower chromitite (Nicholson and Mathez 1991; Smith *et al.* 2021). The thickness  
157 of this anorthosite “bleached zone” apparently positively correlates with the thickness of the  
158 lower chromite (Nicholson and Mathez 1991). In parts of the western lobe (*e.g.*, Turfspruit and  
159 Wolhunderskop), the anorthosite may be mottled (*i.e.*, containing large oikocrysts of olivine  
160 and pyroxene) or spotted (*i.e.*, containing equant pyroxene crystals interpreted to be of  
161 cumulus origin) (Maier and Eales 1997). In the eastern limb (*e.g.*, Winnaarshoek and Atok),  
162 the Merensky Reef sequence is hosted amongst layered norite, gabbronorite, and feldspathic  
163 orthopyroxenite (Cameron 1970; Lee and Butcher 1990; Mathez *et al.* 1997; Mitchell and  
164 Scoon 2007).

165 This study is concerned with normal (relatively thin) Merensky Reef sampled at the  
166 Rustenburg Section of the Rustenburg Platinum Mines (Fig. 1C; Viljoen and Hieber 1986;  
167 Nicholson and Mathez 1991; Wilson *et al.* 1999; Smith *et al.* 2021). At this location, the central  
168 pyroxenite is coarse-grained and ranges from a few cm to up to 1 m in thickness (Viljoen and  
169 Hieber 1986; Wilson *et al.* 1999). This unit is bracketed by two mm-scale chromitite layers.  
170 The upper chromitite is discontinuous and compacted relative to the lower chromitite. The  
171 lower chromitite is underlain by a cm- to dm-scale layer of anorthosite, which in turn, is

172 underlain by barren leuconorite (Wilson *et al.* 1999; Smith *et al.* 2021). The upper chromitite  
173 is overlain by a medium-grained 'hanging-wall' pyroxenite. Disseminated sulfides are  
174 prevalent in the central pyroxenite and chromitites, and they further extend downwards into  
175 the immediate anorthosite footwall as well as concentrate in the lowermost portion of the  
176 hanging-wall pyroxenite (*i.e.*, directly above the upper chromitite).

### 177 3. MATERIALS AND METHODS

178 This study performs microtextural analyses on sections produced from a 30 x 10 x 2 cm  
179 sample (RPM-1) of the Merensky Reef from the Rustenburg Platinum Mine (Fig. 1C) (Smith  
180 *et al.* 2021). Methods are detailed in Electronic Supplementary Material (ESM) 1. Data and a  
181 summary of thermodynamic forward models are given in ESM 2. Raw data files and model  
182 outputs can be accessed from the digital data archive at [doi.org/10.25919/rgb7-ch54](https://doi.org/10.25919/rgb7-ch54).

183 Both EDS and EBSD maps were produced at Cardiff University using a Zeiss Sigma HD  
184 Analytical Field Emission Gun Scanning Electron Microscope equipped with two Oxford  
185 Instruments 150 mm<sup>2</sup> energy dispersive spectrometers and a Nordlys EBSD detector inserted  
186 to 191 mm. The data were subsequently processed using MTEX (Bachmann *et al.* 2010) and  
187 the J-, M-, L#, and F# indices have been used to evaluate mineral fabrics, which were  
188 calculated on their respective orientation density function (ODF) (Bunge 1982; Skemer *et al.*  
189 2005; Mainprice *et al.* 2015; Cheadle and Gee 2017). The ODFs were calculated using a de  
190 la Valée Pousin kernel with a half-width of 10°. Crystal size distribution (CSD) profiles of  
191 chromite were determined using CSDCorrections v1.6 (Higgins 2000).

192 The compositions of silicates (Table 1 and ESM 2) were determined at Camborne School of  
193 Mines (University of Exeter) using a JEOL JXA-8200 electron-probe microanalyzer over four  
194 analytical sessions (ESM 2; [doi.org/10.25919/rgb7-ch54](https://doi.org/10.25919/rgb7-ch54)). Detection limits for Ca, Mg, and K  
195 were below 200 ppm, those for Al, Na, Mn, and P were below 400 ppm, those for Al and Mn  
196 were below 150 ppm, and those for Si, Fe, Cr, and Ti were below 600 ppm. An EPMA map of



197 chromite crystals in the lower chromitite was produced using a Cameca SX-Five EPMA at the  
198 Centre de Microcaractérisation Raimond Castaing (University Paul Sabatier, Toulouse).

199 Chromite compositions (ESM 2) were determined by LA-ICP-MS at LabMaTer, Université du  
200 Quebec, using an Excimer 193 nm resolution M-50 LA system (Australian Scientific  
201 Instrument) equipped with a double volume cell S-155 (Laurin Technic) and coupled with an  
202 Agilent 8900 mass spectrometer. The tuning parameters were a laser frequency of 15 Hz, a  
203 power of 3 mJ/pulse, a dwell time of 7.5 ms, and a fluence of 5 J/cm<sup>2</sup>. The beam size was 44  
204 µm and line scans were carried out across the grains with a stage speed of 10 µm/s. The  
205 ablated material was carried into the ICP-MS by an Ar–He gas mix at a rate of 0.8–1 L/min for  
206 Ar and 350 mL/min for He, and 2mL/min of nitrogen was also added to the mixture. Data  
207 reduction was carried out using the Iolite package for Igor Pro software (Paton et al. 2011).  
208 External calibration was carried out GSE-1g and NIST-610 (supplied by USGS) and results  
209 were monitored using GProbe 6, a basaltic glass, and natural chromite crystals from in-house  
210 reference materials (G-12 G seam Stillwater Complex and BC-16 massive chromite UG2).  
211 The results obtained for the monitors agree within analytical error with the working values  
212 (ESM 2), except for Sc in NIST-616 due to interference from Si. Mineral formulae were  
213 recalculated using GCDKit.Mineral (Janoušek *et al.* 2024).

214

## 215 **4. RESULTS**

### 216 **4.1. Footwall leuconorite**

217 The leuconorite contains ~ 25-30% orthopyroxene, ~ 60-70% plagioclase and traces of  
218 intercumulus clinopyroxene (~ 1-3%) and quartz (~ 0.5-1%). Orthopyroxene crystals (~ 1-5  
219 mm in diameter) are anhedral and possess thin (< 1 mm) poikilitic overgrowths that are often  
220 partially surrounded by intercumulus clinopyroxene (Fig. 2A-B). Accessory chromite crystals  
221 occur at the margins of orthopyroxene oikocrysts throughout the leuconorite, relatively  
222 increasing at the leuconorite-anorthosite contact as well as in proximity to intercumulus  
223 clinopyroxene (ESM 3i), before virtually vanishing above the leuconorite-anorthosite contact.

224 Accessory phlogopite, apatite, and Fe-Ti oxides occur throughout the feldspathic domains.  
225 Sulfide blebs (pyrrhotite-pentlandite-chalcopyrite) with interstitial morphologies are also most  
226 abundant in the uppermost part of the unit, where they are spatially associated with  
227 intercumulus quartz and pyroxenes as well as complexly zoned cumulus plagioclase. The  
228 orthopyroxene crystals have 80.0-78.6 mol.% Mg#, 0.59-0.35 wt.% Cr<sub>2</sub>O<sub>3</sub>, and display normal  
229 compositional zoning whereby Cr<sub>2</sub>O<sub>3</sub> values decrease from core to rim while TiO<sub>2</sub>  
230 concentrations increase (Fig. 3A-B; ESM 2). Cumulus plagioclase crystals (~ 1 mm of  
231 equivalent radius) are subhedral and have An contents ranging from 78.1-71.5 mol.%. They  
232 display no systematic compositional zonation in the studied sections (Fig. 3C).

233 Fabrics for plagioclase and orthopyroxene are not random (Fig. 2C-D). For both phases, the  
234 [010] axes are oriented normal to the compositional layering, while the [100] and [001] axes  
235 form a girdle on the layering plane. The fabric recorded by cumulus plagioclase is relatively  
236 weak (J-index = 1.79), yet comparable to magmatic fabrics recorded by the gravitational  
237 settling of cumulus tabular phases (Satsukawa *et al.* 2013; Holness *et al.* 2017; Cheadle and  
238 Gee 2017). The fabric recorded by orthopyroxene crystals is relatively stronger (J-index =  
239 5.30), though it is likely biased because of the few orthopyroxene crystals sampled as well as  
240 their poikilitic nature.

241 For all phases, only rare indicators of plastic deformation exist, such as sub-grains in  
242 orthopyroxene and plagioclase (Fig. 2E-G). Cumulus plagioclase crystals are extensively  
243 twinned with straight twin boundaries that crosscut the entire crystals. The EBSD data indicate  
244 that the Albite, Carlsbad-A and Albite-Carlsbad-A twin laws make up most of the twin  
245 interfaces in the footwall norite. Investigation of the relationship between orthopyroxene  
246 crystals and their associated interstitial clinopyroxene rims revealed a non-random and  
247 consistent distribution of their crystallographic axis; orthopyroxene [100], [010], and [001]  
248 parallels clinopyroxene [100], [010], and [001], respectively (ESM 3ii). This parallel relationship  
249 between the two pyroxenes suggests that clinopyroxene is using previously existing  
250 orthopyroxene as a crystallization substrate (ESM 3ii).

251 In the upper ~ 1 cm of the leuconorite (*i.e.*, at the contact with the anorthosite), the relative  
252 width of poikilitic orthopyroxene rims increase (ESM 3iii), and cumulus plagioclase crystals  
253 display more complex oscillatory zoning, albeit with An contents (77.1-72.7 mol.%) similar to  
254 those analyzed in the underlying leuconorite (Figs. 3C). On average, orthopyroxene crystals  
255 here have lower Mg# values (79.2-75.5 mol.%) and similar Cr<sub>2</sub>O<sub>3</sub> (0.56-0.24 wt.%)  
256 concentrations relative to those analyzed in the underlying leuconorite (Fig. 3A-B).

#### 257 **4.2. Footwall anorthosite**

258 The anorthosite (~ 3-4 cm thick) forms the immediate footwall to the reef with which it shares  
259 a knife-sharp contact. Its contact with the leuconorite is fairly sharp and marked by an abrupt  
260 decrease in the modal abundance of orthopyroxene (*e.g.*, from 25 to 0.5%). Approximately  
261 95% of the unit consists of subhedral cumulus plagioclase (up to ~ 3 mm in length) that  
262 possess An contents of 78.7-63.8 mol.% and complex oscillatory zoning (Figs. 3D, 4A-B).  
263 Chromite, apatite, and Fe-Ti oxides are accessory phases. Sulfides (~ 1-2%) occur within sub-  
264 vertical domains, together with quartz, pyroxenes, and phlogopite, that traverse the entire  
265 anorthosite and gradually dissipate at the leuconorite-anorthosite contact. The sulfides consist  
266 of fairly equal proportions of pentlandite, chalcopyrite, and pentlandite.

267 Microstructurally, the anorthosite is similar to the leuconorite. The cumulus plagioclase  
268 crystals are subhedral, with long axes that have a tendency to parallel the compositional  
269 layering. The crystals record a weak but non-random fabric with [010] axes that cluster  
270 normally to the layering plane as well as a well-defined girdle for the [100] axes on the layering  
271 plane (J-index = 2.47) (Fig. 4C). Cumulus plagioclase crystals display limited evidence for  
272 internal deformation and similar twin laws to those analyzed in the leuconorite (Fig. 5A-C).

273 Beginning approximately 1 cm beneath the lower chromitite, is a ~ 5-mm-thick layer of  
274 anorthosite that contains clinopyroxene oikocrysts (Mg#<sub>82.6-84.5</sub>; mode ~ 8-10% of this interval)  
275 and interstitial orthopyroxene (~ mode 3-5% of this interval) as well as accessory quartz and  
276 phlogopite (< 1%; Fig. 5A). The intercumulus clinopyroxenes are oikocrysts that record

277 variable degrees of internal misorientation (Fig. 5D-E), consistent with either limited plastic  
278 deformation during late-stage compaction or the growth of complexly-shaped oikocrysts with  
279 large lateral extents. Alternatively, it could be considered as a result of the growth of the  
280 complex shaped oikocrysts – the very large lateral extend for the oikocrysts which span across  
281 the entire width of our sample aligns well with the later.. The uppermost 5 mm of this unit (*i.e.*,  
282 directly below the *lower chromitite*) is an almost pure seam of anorthosite (*bleached zone* of  
283 Nicholson and Mathez (1991), containing coarse-grained plagioclase crystals (up to ~ 8 mm  
284 in length) that extend from the anorthosite into the lower chromitite. Cumulus plagioclase in  
285 these uppermost portions possess [010] axes normal to the layering plane and [100] axes  
286 scattered in a girdle on the layering plane (J-index = 4.66; Fig. 5F). The fabric indices for this  
287 uppermost portion are stronger than those recorded in the underlying leuconorite.

#### 288 **4.3. Lower chromitite and central pyroxenite**

289 The lower chromitite is approximately 1.5 to 3 cm thick and shares a knife-sharp contact with  
290 the underlying anorthosite. The unit consists of ~ 50% chromite, whereby crystals manifest as  
291 (i) relatively coarser amoeboidal crystals that commonly display hook-like features (ESM 3iv;  
292 *cf.* Yudovskaya *et al.* 2019) and enclose polymineralic silicate or sulfide inclusions; and (ii)  
293 relatively finer blocky subhedral crystals that are devoid of inclusions and commonly clustered  
294 (see also Li *et al.* 2005; Vukmanovic *et al.* 2013). The chromite crystals are hosted by  
295 plagioclase oikocrysts (~ 30-35%) in the lower two-thirds of the unit and by orthopyroxene  
296 oikocrysts (~ 20-25%) in the upper third of the unit (Fig. 5A). Rutile is a common accessory  
297 phase in the upper orthopyroxene-hosted portion of the chromitite, whereas accessory  
298 phlogopite, apatite, clinopyroxene, and sulfides occur throughout the chromitite (Fig. 6A-B).  
299 Thick section D1 samples the lower portion of the central pyroxenite, which consists mostly of  
300 coarse-grained orthopyroxene (~ 80-90%) with accessory plagioclase (~ 1-4%; An<sub>68-64</sub>),  
301 clinopyroxene (~ 2-5%), chromite (~ 2-4%), quartz, phlogopite, and sulfides.

302 One plagioclase crystal sampled towards the base of the lower chromitite is strongly reversely  
303 zoned (Fig. 3D); the areas directly adjacent to chromite are 10 mol.% more anorthitic than the

304 remaining transect (see also Smith *et al.* 2021). Orthopyroxene in the chromitite and  
305 pyroxenite are relatively less evolved ( $Mg_{-84}$ ) than those analysed in the footwall, yet with  
306 similar  $Cr_2O_3$  and  $TiO_2$  concentrations. Orthopyroxene analyses proximal to chromite crystals  
307 (< 2 mm) have relatively higher  $Mg_{opx}$  as well as lower Cr and Ti concentrations (Fig. 3A-B).  
308 In contrast to underlying cumulus plagioclase, plagioclase oikocrysts appear to be orientated  
309 with their (010) planes normal to the layering plane and with their a- [100] and c-axis [001]  
310 being scattered on the vertical plane, while orthopyroxene oikocrysts have their (010) planes  
311 coincident to the layering plane. Internal misorientation is observed within the plagioclase  
312 oikocrysts, beginning at the anorthosite-chromitite contact. The orthopyroxene oikocryst within  
313 the chromitite shows some internal misorientation, yet there is little evidence of internal  
314 deformation in the orthopyroxene in the uppermost portion of the chromitite.

315 Regardless of their stratigraphic level and host phase, blocky chromite crystals show no signs  
316 of lattice bending (Fig. 6C-D). Conversely, amoeboidal chromite crystals can either be free of  
317 lattice misorientation or show evidence of extensive lattice bending, where the latter may  
318 resemble subgrains or undulose extinction as observed in non-isotropic minerals. No common  
319 structures for the subgrains were apparent in the amoeboidal chromite. The greatest degree  
320 of lattice bending is observed in crystals that display the most complex and concave crystal  
321 boundaries. Amoeboidal crystals generally have relatively larger equivalent radii (> 0.2 mm)  
322 and crystal orientation spread values (> 1°), making them somewhat distinguishable from  
323 blocky grains. The CSD profile for all lower chromitite crystals is concave at crystal sizes <  
324 0.16 mm and displays a well-defined kink at crystal sizes of ~ 0.38 mm. Crystals with sizes  
325 below 0.38 mm (0.10-0.38 mm) are defined as  $y = -14.3x + 7.5$  ( $r^2 = 0.989$ ) and crystals with  
326 sizes above 0.38 mm kink (0.38-1.21 mm) are defined as  $y = -6.3x + 4.6$  ( $r^2 = 0.999$ ) (Fig. 6E-  
327 F). The concave profile at small crystal sizes is predominantly defined by plagioclase-hosted  
328 crystals, while the kink is best displayed in orthopyroxene-hosted crystals.

329 Semi-quantitative EDS element maps show that chromite Cr# and Ti contents increase  
330 upwards through the lower chromitite, while Mg# values decrease upwards (Fig 7A-C). More

331 specifically, it appears that chromite crystals hosted by, or proximal to, orthopyroxene have  
332 relatively higher Cr# and lower Mg# contents. However, this is not always the case and would  
333 need to be examined in three dimensions. A high-resolution EPMA element map (Fig. 7D)  
334 shows that there are no obvious chemical differences between amoeboidal and blocky crystals  
335 and it appears that the portion of mapped amoeboidal crystal submerged by orthopyroxene  
336 has relatively higher TiO<sub>2</sub> and Fe<sub>2</sub>O<sub>3</sub> contents, as well as relatively lower Cr<sub>2</sub>O<sub>3</sub> contents. There  
337 is no discernible chemical gradation in the plagioclase-hosted amoeboidal crystal.

338 There is negligible inter- and intra-grain chemical variation in lower chromitite crystals,  
339 including between amoeboidal and blocky subtypes (Table 2; Fig. 8). The chromite crystals  
340 have 29.6-34.7 mol.% Mg#, 64.8-70.3 mol.% Cr#, and 1.3-2.6 wt.% TiO<sub>2</sub>. In general, Mg#  
341 contents decrease with increasing Cr# contents; plagioclase-hosted crystals have higher Mg#  
342 and lower Cr# contents, whereas orthopyroxene-hosted crystals in the uppermost portion  
343 have lower Mg# and higher Cr# contents. Chromite crystals in the latter group have  
344 compositions that are somewhat intermediary between lower and upper chromitite crystals.  
345 Vanadium and Mn concentrations increase with decreasing Mg# contents, whereas Sc and  
346 Ga decrease with decreasing Mg# contents.

#### 347 **4.4. Upper chromitite and base of the hanging-wall pyroxenite**

348 The upper chromitite is much thinner (< 0.5 cm), more equilibrated, and less continuous  
349 relative to the lower chromitite (Fig. 6A-B). Our section samples the upper chromitite in two  
350 parts that have relatively different appearances. The portion underlying a large clinopyroxene  
351 oikocryst possesses highly compacted blocky chromite grains with negligible amounts of  
352 interstitial silicates that collectively are bound by orthopyroxene and phlogopite (Fig. 6B). The  
353 other portion comprises weakly compacted chromite grains (~ 55-60%) associated with  
354 plagioclase oikocrysts (~ 12-15%) as well as intercumulus clinopyroxene (~ 2-3%), quartz (~2-  
355 4%), phlogopite (< 1%), and rutile (~2-3%). Sulfides are disseminated throughout this unit (~  
356 4-5%).

357 Chromite crystals are generally blocky, yet there are few non-blocky grains that record large  
358 degrees of internal misorientation (Fig. 6C-D). The CSD profile of upper chromitite crystals is  
359 distinct from those of the lower chromitite in that there is no subtle fan-shaped array at larger  
360 grain sizes ( $> 0.2$  mm; Fig. 6E). Like lower chromitite CSD profiles, however, there is a slight  
361 convex concave pattern at smaller grain sizes ( $< 0.2$  mm), which is consistent with small  
362 degrees of Ostwald Ripening (Marsh 1988).

363 There is negligible inter- and intra-grain chemical variation in upper chromitite crystals. The  
364 chromite crystals have 23.4-26.2 mol.% Mg#, 71.8-75.0 mol.% Cr#, and 2.7-3.3 wt.%  $\text{TiO}_2$ .  
365 The single plagioclase-hosted crystal has the lowest Cr# and highest Mg# values measured  
366 in this unit. Like the lower chromitite crystals, Mg# values decrease with increasing Cr# values;  
367 however, upper chromitite crystals have statistically significantly lower Mg# and higher Cr#  
368 concentrations (Fig. 8). Moreover, upper chromitite crystals have higher V, Sn, and Mn  
369 concentrations than lower chromitite crystals.

370 The hanging-wall pyroxenite is a medium-grained orthopyroxenite with no obvious  
371 compositional or graded layering. It comprises an interconnected network of subhedral  
372 cumulus orthopyroxene ( $\sim 65$ -75%) and intercumulus plagioclase ( $\sim 15$ -25%) with traces of  
373 interstitial clinopyroxene, phlogopite, quartz, and sulfides (ESM 3v). Clinopyroxene sometimes  
374 occurs as relatively coarse-grained oikocrysts (up to 1 cm in diameter). As in the central  
375 pyroxenite, EPMA analyses of orthopyroxene at the base of the hanging-wall pyroxenite show  
376 it to be relatively Mg-rich and Cr-poor where proximal to chromite (Fig. 3A-B). The base of the  
377 unit contains very few chromite crystals and a relatively high proportion of sulfides that consist  
378 of loop-textured pentlandite encircling pyrrhotite and associated chalcopyrite.

379 The fabric of cumulus orthopyroxene yields a similar crystallographic preferred orientation  
380 (CPO) to that measured in the footwall silicates and conserves a similar orientation for the  
381 [010] axes (J-index = 2.74; Fig. 9). As in the footwall, internal misorientation is very limited and  
382 pristine magmatic textures are preserved. Clinopyroxene and intercumulus plagioclase do not

383 show extensive markers for plastic deformation, with only rare sub-grains and lattice bending  
384 being visible at contacts with other phases.

385

## 386 5. DISCUSSION

### 387 5.1. Deposition of the footwall leuconorite

388 The footwall leuconorite is typical of *Upper Critical Zone* norite in that it comprises laminated,  
389 subhedral cumulus plagioclase crystals with subhedral orthopyroxene oikocrysts, adjacent to  
390 which intercumulus clinopyroxene generally occurs (Fig. 2B; Eales *et al.* 1991; Maier and  
391 Eales 1997; Boorman *et al.* 2004). The weak magmatic fabric exhibited by undeformed  
392 cumulus plagioclase is evidence for igneous lamination, whereas there is little evidence for  
393 lineation (*e.g.*, absence of maxima at the [100] axis; Cheadle and Gee 2017). Similar fabrics  
394 have been recorded in cumulus plagioclase-bearing units of the Skaergaard (Holness *et al.*  
395 2017), Rum (Cheadle and Gee 2017), and Stillwater (Jenkins *et al.* 2022) intrusions as well  
396 as elsewhere in the Bushveld Complex (Vukmanovic *et al.* 2019; Smith *et al.* 2023).  
397 Orthopyroxene oikocrysts define a fabric that is like that of cumulus plagioclase, indicating that  
398 both silicates record the same magmatic event. The evidence is consistent with cumulus  
399 plagioclase and, by extension, orthopyroxene having accumulated through gravitational  
400 settling in a stagnant or weakly-flowing melt (Henry *et al.* 2021), followed by postcumulus  
401 overgrowth of orthopyroxene (Barnes *et al.* 2016). Evidence for minor plastic deformation  
402 occurred later as a result of crystal loading and compaction of the cumulates (Henry *et al.*  
403 2021).

404 Cumulus plagioclase crystals show no systematic compositional zoning or change in  
405 composition with proximity to the anorthosite (Fig. 10A). However, their compositional zoning  
406 patterns diversify at the leuconorite-anorthosite contact (Fig. 4B). This occurs in conjunction  
407 with orthopyroxene oikocrysts with relatively lower  $Mg\#_{opx}$  values (Fig. 3A) as well as a relative  
408 increase in the modal abundance of clinopyroxene and accessory phases (Fig. 11A). This



409 pattern in  $Mg\#_{\text{opx}}$  has been reported in the footwall units at the Union, Impala Platinum, and  
410 Rustenburg Mines (Naldrett *et al.* 1986; Schurmann 1993; Cawthorn 1996). Wilson *et al.*  
411 (1999) did not identify this trend in a sequence without the footwall anorthosite at the  
412 Rustenburg Platinum Mine but did highlight that  $Mg\#_{\text{opx}}$  decreases as whole-rock Zr contents  
413 increase. This trend was initially ascribed to differentiation (Naldrett *et al.* 1986; Schurmann  
414 1993; Maier and Eales 1997), yet as An content remains constant, it was later proposed to be  
415 a result of re-equilibration with variable portions of trapped liquid (Cawthorn 1996; Wilson *et*  
416 *al.* 1999).

417 Zoning of  $Mg^{2+}$  and  $Fe^{2+}$  is not often preserved in ferromagnesian cumulates of layered  
418 intrusions due to the rapid diffusion rates of these divalent elements (Barnes *et al.* 2016). In  
419 contrast,  $Cr^{3+}$  and  $Ti^{4+}$  diffuse relatively slowly, such that any zoning of these elements could  
420 be preserved. For this reason, Barnes (1986b) argued that orthopyroxene-rich cumulates with  
421 variable Cr contents for a narrow Mg# range are probably the result of differentiation, whereas  
422 orthopyroxene-rich cumulates with narrow Cr contents for a variable Mg# range are probably  
423 the result of variable degrees of trapped liquid shift. The effect of trapped liquid shift between  
424 60:40 mixtures of measured plagioclase ( $An_{80}$ ) orthopyroxene ( $Mg_{81}$ ) and variable proportions  
425 of evolved B1 melt (ECBV105 of Barnes *et al.* 2010) was tested by modelling batch  
426 crystallization of spinel-free hypothetical cumulates close to their solidus at 2 kbar and  $\Delta FMQ$   
427 using alphaMELTS 1.9 (Ghiorso and Sack 1995; Jenkins and Mungall 2018). The final vector  
428 is drawn by connecting the original and final 're-equilibrated' orthopyroxene compositions (see  
429 supplementary materials).  $\log D_{Cr}^{\text{opx/liq}}$  was parametrized as  $-4.59 + 8100 / \text{Temperature (K)}$   
430 and  $D_{Cr}^{\text{cpx/liq}}$  was taken as  $1.7 \times D_{Cr}^{\text{opx/liq}}$  (following Barnes 1986a; 1986b).

431 Results of the modelling show that  $Mg\#_{\text{opx}}$  can be lowered 1.0, 3.6, and 7.1 mol.% in the  
432 presence of 5%, 10%, and 20% trapped liquid, respectively, and Cr contents slightly decrease  
433 (Fig. 12), consistent with the results of Barnes (1986b). Orthopyroxene crystals from the  
434 leuconorite have variable Cr contents for narrow  $Mg\#_{\text{opx}}$  values, consistent with the effects of  
435 differentiation and subsequent  $Mg^{2+}$ - $Fe^{2+}$  diffusion (Barnes 1986b). The relatively lower  $Mg\#_{\text{opx}}$

436 values for orthopyroxene crystals at the leuconorite-anorthosite contact can, therefore, be  
437 ascribed to orthopyroxene re-equilibrating with up to 10% trapped liquid. These results are  
438 consistent with the observed increase in the modal abundance of intercumulus pyroxene and  
439 accessory minerals at this transition as well as modal trapped liquid estimates for the Upper  
440 Critical Zone norite (1-10%; Cawthorn and Walsh 1988; Cawthorn 1996; Wilson *et al.* 1999;  
441 Yao *et al.* 2021). Moreover, as disseminated sulfides subtly concentrate directly above the  
442 leuconorite, the composition of orthopyroxene may have been further influenced by Fe-Ni  
443 exchange with sulfide melt, though we presently do not have the data to confirm this.

## 444 **5.2. Formation of the footwall anorthosite**

445 In many parts of the western lobe of the Bushveld Complex, the Merensky Reef is underlain  
446 by an anorthosite of variable thickness (Eales *et al.* 1988; Viring and Cowell 1999). In the  
447 Critical Zone, anorthosite typically occurs at the top of interlayered packages of pyroxenite,  
448 norite, and anorthosite (Kruger and Marsh 1985; Eales *et al.* 1986; Maier and Eales 1997;  
449 Cawthorn 2002; Seabrook *et al.* 2005; Veksler *et al.* 2015; Hunt *et al.* 2018). As a result,  
450 anorthosite layers are often overlain by PGE-rich chromitite seams that tend to occur at the  
451 base of these units (Eales *et al.* 1990; Scoon and Teigler 1995; Van der Merwe and Cawthorn  
452 2005; Maier and Barnes 2024). This spatial association between anorthosite and chromitite is  
453 recognized in other layered intrusions, such as Rum (Scotland; O'Driscoll *et al.* 2009),  
454 Stillwater (USA; Marsh *et al.* 2021), and Penikat (Finland; Maier *et al.* 2018). The origin of the  
455 Critical Zone cycles has been ascribed to magma replenishment, during which the  
456 replenishing melt(s) may have thermally, mechanically, and (or) chemically interacted with  
457 resident cumulates (Eales *et al.* 1986, 1988; Maier and Eales 1997; Viljoen 1999; Roberts *et*  
458 *al.* 2007; Scoon and Costin 2018; Mitchell *et al.* 2019; Kruger and Latypov 2021; Latypov *et*  
459 *al.* 2022).

460 In this study, the anorthosite is relatively thin compared to footwall anorthosite elsewhere at  
461 the Rustenburg Platinum Mines (Viljoen and Hieber 1986; Eales *et al.* 1988). Cumulus  
462 plagioclase at the base of the anorthosite displays normal, reverse, and oscillatory zoning,

463 whereas plagioclase crystals directly beneath the lower chromitite are often reversely zoned  
464 (Figs. 3D and 4B). Reversely zoned plagioclase are commonplace in the Upper Critical Zone  
465 (Maier 1992; Maier and Eales 1997; Robb and Mungall 2020, Maier *et al.* 2021), and it appears  
466 to become most pronounced in 'pure' anorthosite rind that occurs directly beneath the lower  
467 chromite (Smith *et al.* 2021; Latypov *et al.* 2023); a feature also described encircling boulders  
468 of the Boulder Bed (Smith *et al.* 2023) and in the Medium-Grained Anorthosite member of the  
469 Stillwater Complex (Baker and Boudreau 2019). This diversity of plagioclase zoning provides  
470 evidence of a complex and changing melt composition in this layer compared to the underlying  
471 leuconorite, which has relatively limited zoning of cumulus plagioclase. In the leuconorite, the  
472 weakly laminated and largely undeformed plagioclase crystals, with no discernible lineation,  
473 are consistent with crystal settling in a quiescent melt column (Cheadle and Gee 2017).  
474 However, the strength of the plagioclase lamination increases upwards through the footwall  
475 anorthosite (*i.e.*, towards the lower chromitite; Fig. 10B-C) and this requires further  
476 explanation.

477 Sinuous networks of sulfides and intercumulus pyroxenes traverse the anorthosite and blanket  
478 the leuconorite (Fig. 11A; Cawthorn 1999; Barnes and Maier 2002; Godel *et al.* 2006; Naldrett  
479 *et al.* 2009; Smith *et al.* 2021). This is compelling evidence that the anorthosite was relatively  
480 permeable at the time of sulfide melt percolation, while the underlying leuconorite was virtually  
481 solidified (Smith *et al.* 2021). Intercumulus pyroxenes, quartz, and phlogopite are relatively  
482 abundant in the uppermost centimeter of the leuconorite and remain abundant throughout the  
483 sinuous networks (Fig.11A). Very fine-grained chromite occurs at the margins of  
484 orthopyroxene crystals throughout the upper leuconorite and, though less frequent, persist in  
485 the sinuous networks (Fig. 11). These crystals may form during the dissolution of Cr-bearing  
486 orthopyroxene (Marsh *et al.* 2021) and may then themselves dissolve as the reaction with  
487 replenishing melt progresses – their persistence in the sinuous networks is evidence that Cr  
488 is mobile. The footwall anorthosite has ~ 1% sulfide, and so the downward percolation of  
489 sulfide melt cannot alone account for the upward migration of relatively larger proportions of

490 trapped silicate melt. As such, we hypothesize that relatively buoyant Cr-bearing silicate melt  
491 generated during this reaction migrated upwards, aided by the downward percolation of  
492 relatively dense sulfide melt. Several studies of the Merensky Reef have shown that  
493 incompatible trace element concentrations peak stratigraphically above peaks in chalcophile  
494 element concentrations (Lee 1983; Cawthorn 1996; Wilson *et al.* 1999; Barnes and Maier  
495 2002), which has also been ascribed to the upward displacement of evolved silicate melt aided  
496 by down-going sulfide melt (Cawthorn and Boerst 2006).

497 Our observations indicate that the anorthosite seemingly cannot be explained by gravitational  
498 processes alone. Instead, the data are more consistent with a model whereby the anorthosite  
499 formed as a restite of partial melting during chamber replenishment (Eales *et al.* 1988; Roberts  
500 *et al.* 2007; Mungall *et al.* 2016). This process could generate enhanced porosity allowing for  
501 the migration of sulfide and silicate melts. One-dimensional heat flow models (Ehlers 2005)  
502 indicate that a stagnant melt at 1300°C is not able to raise the temperature of floor rocks above  
503 1200°C unless the floor rocks are already hot (> 1000°C) and (or) the melt column is  
504 excessively hot (> 1500°C) or thick (> 1 km). Thus, for melting to proceed, the heat of the  
505 overlying melt must be sufficiently sustained for prolonged periods of time via continuous  
506 replenishment. It should be noted that alternative models have been proposed for the  
507 anorthosite underlying the Merensky Reef, including reactive porous flow (Nicholson and  
508 Mathez 1991; Mathez 1995; Marsh *et al.* 2021; Maier *et al.* 2021).

509 To provide additional constraints on the viability of footwall melting by replenishing melt, a  
510 series of assimilation-fractional crystallization thermodynamic models at 2 kbar pressure were  
511 performed using Magma Chamber Simulator (Bohrson *et al.* 2014, 2020). The replenishing  
512 melt was modelled as B1 or 60:40 B1:B2 (Table 2; Barnes and Maier 2002; Barnes *et al.*  
513 2010), which were both equilibrated at  $\Delta$ FMQ. The footwall compositions were taken from data  
514 of Maier and Eales (1997) who studied the UG2-Merensky Reef interval along strike in the  
515 western lobe. These included: (i) leuconorite (Inor) with ~ 3.5 wt.% MgO (average of Union  
516 647.9, 649.4, and 652.9); (ii) norite (nor) with ~ 8.6 wt.% MgO (average of IN 811.73, LK7

517 1389.7, EK 22 272.25, and H3 1054.1); (iii) melanorite (mnor) with 11.6 wt.% MgO (mnor;  
518 average IM 801, 810.1, and 818); (iv) highly melanocratic (mnor2) norite with 17.6 wt.% MgO  
519 (IM788.8 at Impala IM). Prior to modelling, FeO/Fe<sub>2</sub>O<sub>3</sub> was calculated for each footwall  
520 composition at 800°C and ΔFMQ, and hydrous equivalents (denoted as *h*-) with ~ 2 wt.% H<sub>2</sub>O  
521 were also produced (Table 2). At the beginning of the simulations, each floor rock was set  
522 slightly above solidus temperature so that 8-10 wt.% of interstitial melt was present – 10 wt.%  
523 of interstitial melt was set as a percolation threshold for the floor rock melt to exit the residue.  
524 Since in Magma Chamber Simulator all heat is distributed evenly in an input mass of wall rock  
525 (here floor rock), we varied its initial mass between 10-50 units (relative to initial melt mass of  
526 100 units, *i.e.*, melt:footwall ratios of 10-2). This can be considered to simulate gradational  
527 changes in footwall composition due to uneven heat distribution. In nature, the thickness of  
528 the affected zone is governed by kinetic processes (such as conduction) that are not  
529 considered by thermodynamics modeling. Simulations with low floor rock mass correspond to  
530 situations of inefficient heat conduction and melting processes taking place in the close vicinity  
531 of the replenishment magma. Each simulation was conducted using 2-5°C temperature  
532 decrements for the replenishment magma. The models with 2 °C decrements were preferred  
533 because they provided a better resolution to study the melting reactions in the footwall. Larger  
534 decrements were used for simulations with higher floor rock mass, where such resolution was  
535 not crucial. The results are summarized in Table 3 and complete model output files are  
536 provided in the online supplementary repository.

537 Leuconorite and norite floor rocks may react with replenishing melts to form an anorthositic  
538 restite, particularly when the system is water-poor, when there is a relatively small volume of  
539 reactive floor rock, or when the replenishing melt is relatively primitive (B1; Fig. 13A-D). The  
540 resulting restite comprises 84.6-99.7% plagioclase (An<sub>80-90</sub>) with accessory olivine (Fo<sub>88-94</sub>) and  
541 Cr-spinel (Table 3). The relative proportions of olivine and Cr-spinel increase in water-rich  
542 scenarios and when the replenishing melt is relatively primitive. Olivine progressively replaces  
543 orthopyroxene in the residue and will later itself become consumed as the reaction progresses.

544 In each scenario, the replenishing melt first becomes saturated in orthopyroxene ( $Mg_{85-88}$ ) and  
545 then Cr-spinel. The initial floor rock melts that form contain ~ 0.84 and 6.0 wt.%  $H_2O$  for water-  
546 poor and water-rich scenarios, respectively. Such water combined with any halogens liberated  
547 from accessory phases (e.g., apatite, mica, amphibole), although not considered in the  
548 simulations, may constitute a burst of volatiles at the level of the nascent Merensky Reef  
549 (Boudreau *et al.* 1986). The absence of olivine at the study location suggests that the system  
550 was relatively dry and (or) that the olivine was consumed by some reaction. The latter is  
551 feasible considering the inferred heightened proportion of trapped melt (Fig. 12) as well as the  
552 presence of quartz, clinopyroxene, and spinel – products in reactions between plagioclase  
553 and ferromagnesian minerals.

554 It is emphasized that although the used modeling scenario was assimilation-fractional  
555 crystallization, we did not aim to model the assimilation process itself, nor its consequences  
556 to the replenishment melt. The focus was on how the heat (both sensible and latent) released  
557 by the crystallizing replenishing melt could modify the resident cumulates. Possible blanketing  
558 of the resident cumulates by crystallization does not significantly hinder this process because  
559 the reaction zone appears to be quite thin (cm-scale), whereas the replenishing melt is  
560 presumed to be at least 20 m thick (see *Section 5.4*). It is argued that the sinuous channels  
561 record intercumulus melt exchange between the melt column and underlying porous  
562 cumulates and, as such, some crystals had likely formed at the cumulate-melt interface as this  
563 reaction progressed. This is further supported by evidence for trapped liquid shift in the reef  
564 stratigraphy as discussed in *Section 5.5*.

565 In summary, resident leuconoritic cumulates can readily react with replenishing melt to  
566 become anorthosite restite. This is regardless of the water concentration of the system, the  
567 volume of reactive cumulates, or the nature of the replenishing melt. Anorthosite restites may  
568 also derive from more noritic cumulates, yet the higher degrees of consumption required may  
569 only be attained when there are small volumes of floor rocks that react (< 20 g of cumulate to

570 100 g of replenishing melt) or when the temperature of the overlying melt is sustained for  
571 extended periods, perhaps by way of progressive replenishment.

### 572 **5.3. Formation of alternative lithologies underlying the Merensky Reef**

573 Anorthosite is not the only lithology that underlies the Merensky Reef. In the NW and SE of  
574 the western lobe of the Bushveld Complex, the Merensky Reef is underlain by troctolite and  
575 olivine norite (Viring and Cowell 1999; Roberts *et al.* 2007). At Northam, Roberts *et al.* (2007)  
576 ascribed the formation of olivine-bearing footwall lithologies to the reconstitution of norite floor  
577 rocks by relatively primitive downward-percolating melt, in a process they termed  
578 *troctolitization*. During troctolitization, Cr- and S-saturated B1 melt percolates downward into  
579 footwall leuconorite, where it consumes orthopyroxene and precipitates olivine that will later  
580 become encased in peritectic orthopyroxene (Roberts *et al.* 2007). Regardless of the true  
581 mechanism, reconstitution of noritic-gabbroic cumulates to troctolite may operate in layered  
582 intrusions. Examples include: (1) the selvage of troctolite around norite-hosted iron-rich  
583 ultramafic pegmatites (Bushveld; Reid and Basson 2002); (2) troctolites in Olivine-bearing  
584 Zone I of the Stillwater Complex may have formed by fluid-induced incongruent melting of  
585 gabbronorite (Boudreau 1999) or as fractionated cumulates of hybridised melt generated as  
586 replenishing melt assimilated partial melts of resident gabbronorite (Jenkins *et al.* 2021); (3)  
587 troctolite at the Wavy Horizon of the Rum intrusion may have formed by dissolution of  
588 clinopyroxene by infiltrating melt (Holness *et al.* 2007). Moreover, in parts of the eastern lobe,  
589 the Merensky Reef is underlain by variably feldspathic orthopyroxenite (Mathez *et al.* 1997;  
590 Mitchell *et al.* 2019). Below we discuss the conditions under which olivine norite, troctolite, and  
591 orthopyroxenite restites may be produced during chamber replenishment (Table 3).

592 Norite residues can remain in water-poor scenarios, where noritic or melanoritic floor rocks  
593 react with relatively evolved replenishing melt (60:40 B1:B2) and all clinopyroxene is  
594 consumed (Fig. 13C, I). In water-rich scenarios and (or) scenarios considering B1 replenishing  
595 melt, olivine norite restites are produced as noritic or melanoritic floor rocks are consumed  
596 (Fig. 13B, E, F, H). These residues contain variable proportions of olivine ( $F_{084-91}$ ),

597 orthopyroxene ( $Mg_{85-91}$ ), and plagioclase ( $An_{80-86}$ ), with accessory Cr-spinel. Troctolite  
598 residues are produced when all orthopyroxene has been replaced by olivine. This occurs in  
599 scenarios where noritic or melanoritic floor rocks react with replenishing melt, particularly when  
600 the system is water-rich and when the replenishing melt is relatively primitive (Fig. 13D, E, G,  
601 H). The troctolite restite contains variable proportions of olivine ( $Fo_{84-93}$ ) and plagioclase ( $An_{85-}$   
602  $90$ ) with accessory Cr-spinel and in some cases orthopyroxene ( $Mg_{85-90}$ ) where not fully  
603 replaced by olivine. These results support the interpretations of Roberts *et al.* (2007) and  
604 further demonstrate that olivine-bearing floor rocks can be generated without the need for  
605 downward melt percolation. It remains possible that reconstituted troctolitic cumulates can be  
606 subjected to a second phase of replenishment-driven reconstitution to produce anorthositic  
607 cumulates, like that proposed for the JM Reef of the Stillwater Complex (Jenkins *et al.* 2021).  
608 Orthopyroxenite and feldspathic orthopyroxenite restites may be produced when replenishing  
609 melts react with melanorite floor rocks that have orthopyroxene:plagioclase ratios above 1  
610 (Fig. 13I, J). To make orthopyroxenite, the system must be relatively water-poor to avoid the  
611 precipitation of significant proportions of olivine, which would instead lead to the formation of  
612 olivine-orthopyroxenite or harzburgite. Residual orthopyroxenite contains 87-96%  
613 orthopyroxene ( $Mg_{87-88}$ ), with accessory Cr-spinel (< 5%), olivine ( $Fo_{86-89}$ ), and plagioclase  
614 ( $An_{86}$ ). The rarity of orthopyroxenite directly beneath the Merensky Reef perhaps reflects the  
615 rarity of *Upper Critical Zone* norites with orthopyroxene:plagioclase ratios above 1.

#### 616 **5.4. Implications for the formation of the lower chromitite and its bimodal chromite** 617 **population**

618 The origin of chromitites in layered intrusions remains intensely debated (Barnes *et al.* 2022;  
619 Latypov *et al.* 2024). It is likely that thin chromitite seams, such as the Merensky chromitites,  
620 form in a different manner from that of massive chromitites (Scoon and Costin 2018; Barnes  
621 *et al.* 2022). Some thin chromitites likely form when replenishing silicate melts (or upwelling  
622 volatiles) interact with resident cumulates, liberating auxiliary  $Al^{3+}$  and  $Cr^{3+}$  from the cumulates  
623 to instigate chromite supersaturation (Boudreau *et al.* 1986; Nicholson and Mathez 1991;



624 O'Driscoll *et al.* 2009; Scoon and Costin 2018; Marsh *et al.* 2021). Such a model could explain  
625 the abundant very fine-grained chromite crystals in the footwall leuconorite that abruptly vanish  
626 at the contact with footwall anorthosite, with the exception of a few crystals residing in sinuous  
627 networks (Fig. 11). Using the mass balance approach of Campbell and Murck (1993),  
628 orthopyroxene from 38 m of leuconorite would need to be consumed to produce a 2-cm-thick  
629 chromitite (80% chromite with 40 wt.% Cr<sub>2</sub>O<sub>3</sub>) at 50% Cr<sub>2</sub>O<sub>3</sub> extraction, while alternatively only  
630 23 m of 60B1:40B2 melt is required to form that same 2-cm-thick chromitite. In the absence  
631 of evidence for cumulate melting to this degree (*i.e.*, the anorthosite is relatively thin at the  
632 subject locality), it would seem that replenishing melts exert the dominant control on chromite  
633 crystallization, which may be later bolstered by Cr<sup>3+</sup> and Al<sup>3+</sup> liberated from the resident  
634 cumulates. Our thermodynamic modelling shows that residual Cr-spinel is produced in each  
635 scenario of footwall reconstitution, particularly in water-rich scenarios (Fig. 13) and that Cr-  
636 spinel will saturate in the replenishing melt shortly after orthopyroxene, further supporting a  
637 potential dual origin for the lower chromitite.

638 As described in other studies (Hulbert and Von Gruenewaldt 1985; Vukmanovic *et al.* 2013;  
639 Yudovskaya *et al.* 2019) and demonstrated in the bimodal CSD profile (Fig. 6E, F), the lower  
640 chromitite of the Merensky Reef hosts two chromite populations - blocky and amoeboidal  
641 chromite (Fig. 6). Blocky crystals are devoid of composite inclusions (*i.e.*, grain porosity) and  
642 lack evidence for internal misorientation, whereas amoeboidal crystals host abundant  
643 composite inclusions and display evidence for a significant degree of internal misorientation.  
644 Hulbert and Von Gruenewaldt (1985) proposed that amoeboidal crystals could form through  
645 solid-state sintering of initially isolated crystals within a reactive Mg-rich liquid. While sintering  
646 is an important postcumulus process in layered intrusions (Hunt *et al.* 2021), the textural (Fig.  
647 6) and chemical (Fig. 7, 8) characteristics of the studied chromite crystals are consistent with  
648 the amoeboidal crystals being single crystallographic entities that must have been  
649 subsequently reworked by some process.

650 In a previous study, Vukmanovic *et al.* (2013) postulated that amoeboidal crystals are  
651 recrystallized dendritic crystals that initially formed via supercooling near the interface  
652 between hot replenishing melt and cool resident cumulates. The misorientation recorded in  
653 the crystal lattices of amoeboidal crystals was ascribed to plastic deformation driven by  
654 compaction. Our sample of the Merensky Reef displays pristine magmatic textures in its  
655 footwall (Figs. 2, 4, and 9) and records no evidence for significant plastic deformation.  
656 Observations of chromite behavior during the plastic deformation of chromitiferous peridotites  
657 suggest that deformation concentrates in the less competent silicates, leaving chromite  
658 relatively undeformed (Holtzman *et al.* 2003; Xiong *et al.* 2017). If plastic deformation was the  
659 sole cause of the observed internal misorientation in crystals of the lower chromitite,  
660 deformation would have disproportionately concentrated in the silicate oikocrysts. Although  
661 the oikocrysts do show some internal misorientation and deformation twins (Fig. 5), taken with  
662 their well-defined CPO, these observations are consistent with only small degrees of  
663 compaction that is insufficient to explain misorientation in the amoeboidal chromite crystals.  
664 Studies of experimental growth of dendrites and skeletal chromite in ophiolites both  
665 demonstrate that misorientation in chromite crystals may result from catastrophic crystal  
666 growth (Sémoroz *et al.* 2001; Griffiths *et al.* 2023; Henry *et al.* 2024), which fits the context of  
667 the Merensky Reef (Vukmanovic *et al.* 2013). We concur with Vukmanovic *et al.* (2013) that  
668 amoeboidal chromite crystals initially formed as skeletal crystals that grew rapidly at the  
669 interface between hot replenishing melt and cool resident cumulates. The amoeboidal shape  
670 arises during a subsequent episode of dissolution-reprecipitation where any misorientation is  
671 an artefact of the initial skeletal state (*cf.* Yudovskaya *et al.* 2019). This episode of dissolution-  
672 reprecipitation may also contribute to the formation of the blocky chromite population.

### 673 **5.5. Chemical diffusion and evidence for evolved trapped liquid in the reef**

674 Cumulus orthopyroxene crystals adjacent to chromite (Fig. 3A-B) record relatively high  $Mg\#_{\text{opx}}$   
675 values and lower Cr concentrations. This compositional change is consistent with subsolidus  
676  $Fe^{2+}-Mg^{2+}$  and  $Cr^{3+}-Al^{3+}$  exchange between chromite and orthopyroxene (Irvine 1967; Sack

677 1982; Hatton and Von Gruenewaldt 1985; Eales and Reynolds 1986). Although not  
678 quantitative, this is broadly consistent with the observed upward increase in chromite Cr# and  
679 Mg# values throughout the lower chromitite (Fig. 7), where those relatively Mg- and Al-poor  
680 crystals in the uppermost portion have compositional similarities with upper chromitite crystals  
681 (Fig. 8). The upper chromitite crystals and those form the uppermost part of the lower  
682 chromitite are relatively Ti-rich and associated with abundant accessory rutile (Fig. 7).

683 With that being said, a high-resolution element map of an amoeboidal chromite at the  
684 plagioclase-orthopyroxene oikocryst grain boundary reveals no systematic chemical changes  
685 with crystal shape or proximity to orthopyroxene (Fig. 7D). In conclusion, postcumulus  
686 diffusion likely augmented chemical gradations in the Merensky chromitite, yet it remains  
687 plausible that these chemical gradations relate to primary crystal growth. For example, Ti could  
688 diffuse between orthopyroxene and chromite; however, there is no correlative Ti-depletion in  
689 orthopyroxene and tetravalent elements diffuse relatively slowly. The relatively Ti-rich  
690 chromite and abundance of accessory rutile are better interpreted as having crystallized from,  
691 or interacted with, relatively evolved trapped liquid, which itself may have been liberated from  
692 the noritic floor rocks. Poikilitic orthopyroxene in the footwall leuconorite has 1000-1500 ppm  
693 Ti (highest in the rims), which when liberated together with Ti from accessory clinopyroxene  
694 and chromite (Fig. 11A) might be sufficient to explain the observed Ti distribution. Of further  
695 note is that clinopyroxene oikocrysts in the upper portion of the footwall anorthosite contain  
696 greater Ti concentrations (~ 0.5 wt.%) than intercumulus clinopyroxene of the Lower Critical  
697 Zone (Godel *et al.* 2011).

698 As predicted in thermodynamic forward models, melts liberated from the footwall may be  
699 initially evolved and potentially rich in volatile species. Previous authors have remarked on the  
700 occurrence of hydrous accessory phases and occasional graphite in the reef (Ballhaus 1988;  
701 Boudreau *et al.* 1986; Li *et al.* 2005), and phlogopite is a common accessory phase in the  
702 presently studied rocks, even partially bounding the upper chromitite (Fig. 6B). This  
703 observation combined with the relatively Al- and Mg-poor nature of the upper chromitite

704 crystals (Fig. 8A; Barnes *et al.* 2022) is consistent with the coexistence of an evolved trapped  
705 melt. Magmatic differentiation would produce a trend of upward decreasing Cr# and Mg#  
706 values of chromite, as observed in Lower Zone chromitites (Hatton and von Gruenewaldt  
707 1985; Scoon and Teigler 1995; Naldrett *et al.* 2009). Conversely, in Merensky Reef and UG2  
708 chromitites, Cr# values of chromite crystals as well as Ti, V, and Fe<sup>3+</sup> concentrations increase  
709 with decreasing Mg# values (Fig. 8; Li *et al.* 2005; Vukmanovic *et al.* 2013; Zaccarini *et al.*  
710 2021). This has been interpreted as a product of postcumulus re-equilibration with trapped  
711 liquid (Hatton and von Gruenewaldt 1985; Eales and Reynolds 1986; Yudovskaya and  
712 Kinnaird 2010; Barnes *et al.* 2022), whereby aliquots of trapped melts may have been  
713 preserved as composite inclusions hosted within amoeboidal chromite (Li *et al.* 2005).

#### 714 **5.6. A note on the relative timing of the deposition of the hanging-wall pyroxenite**

715 Several past authors have argued that the hanging-wall pyroxenite was deposited by some  
716 mechanism prior to the formation of the Merensky Reef (Boudreau *et al.* 1986; Nicholson and  
717 Mathez 1991; Hayes *et al.* 2024). However, evidence from the present study is inconsistent  
718 with this conclusion. Firstly, the euhedral crystal shapes, well-defined CPO, and undeformed  
719 nature of the cumulus orthopyroxene crystals in the studied hanging-wall pyroxenite are  
720 consistent with the settling of cumulus crystals from an overlying melt column, which in turn is  
721 consistent with the thickening of this unit in pothole-reef facies (Ballhaus 1988; Roberts *et al.*  
722 2007). Secondly, the concentration of sulfides directly above the upper chromitite (*i.e.*, at the  
723 base of the hanging-wall pyroxenite; Viljoen 1999; Smith *et al.* 2004; Smith *et al.* 2021) is  
724 consistent with the concomitant deposition of cumulus orthopyroxene and sulfide melt, with  
725 the latter having undergone some degree of percolation that was hindered by the presence of  
726 a pre-existing upper chromitite (*e.g.*, Godel *et al.* 2006). Thirdly, the Merensky pegmatoid and  
727 lower chromitite are locally truncated by the hanging-wall pyroxenites (Latypov *et al.* 2015).  
728 Fourthly, whole-rock incompatible trace element concentrations peak directly above the peaks  
729 in chalcophile metals (Cawthorn 1996; Wilson *et al.* 1999; Cawthorn and Boerst 2006), which

730 has been ascribed to the upward displacement of silicate liquid by down-going sulfide melts  
731 and, thus, exchange between the reef interval and the directly overlying cumulates.

732

### 733 **5.7. Anorthosite formation by replenishment-driven footwall reconstitution with** 734 **implications for the formation of the Merensky Reef sequence**

735 It is proposed that the leuconorite in the footwall of the Merensky Reef formed through the  
736 gravitational accumulation of plagioclase and orthopyroxene from a quiescent melt (Fig. 14A).  
737 This is consistent with the weakly laminated and undeformed tabular plagioclase crystals that  
738 record negligible lineation (Fig. 2). The leucocratic nature of the upper portion of so-called  
739 cyclic units likely reflects the difference in settling rates between these phases and, as such,  
740 the resident cumulates may have been locally anorthositic (Cawthorn 2002). These resident  
741 cumulates were later eroded during an episode of chamber replenishment along the base of  
742 the resident magma column, forming the Merensky unconformity (Fig. 14B; Eales 1988;  
743 Cawthorn and Boerst 2006; Latypov *et al.* 2022). Chromite must have been the liquidus phase  
744 of this replenishing melt.

745 At the study location, reaction between replenishing melt(s) and resident cumulates is  
746 recorded in the upper few centimeters of the footwall (*i.e.*, the footwall anorthosite). The first  
747 partial melts liberated from the footwall leuconorite were likely to be relatively volatile-rich and  
748 with some Al<sup>3+</sup> and Cr<sup>3+</sup> released during the eutectic melting plagioclase and orthopyroxene  
749 (O'Driscoll *et al.* 2009; Scoon and Costin 2018; Schannor *et al.* 2018). The introduction of  
750 these components to the overlying melt column triggered Cr-supersaturation (Ballhaus 1988),  
751 and the *in situ* crystallization of skeletal chromite (Vukmanovic *et al.* 2013). Some sulfide  
752 droplets nucleated on these skeletal chromite crystals (Fig. 14C; Barnes *et al.* 2021). The  
753 microtextures of amoeboidal chromite are consistent with dissolution-reprecipitation of  
754 originally skeletal crystals, which demand a period of Cr-undersaturation perhaps triggered by  
755 a subsequent influx of initially Cr-undersaturated melt (Fig. 14D; Yudovskaya *et al.* 2019). The

756 conversion of skeletal to amoeboidal crystals resulted in the entombment of affixed sulfide  
757 droplets (Holwell *et al.* 2011; Hutchinson *et al.* 2015) and evolved interstitial melt (Ballhaus  
758 and Stumpfl 1986; Li *et al.* 2005; Vukmanovic *et al.* 2013), that itself may represent partial  
759 melt liberated from the underlying cumulates. A portion of blocky chromite crystals may form  
760 during the reconstitution of skeletal crystals and (or) subsequently as the overlying melt once  
761 again becomes Cr-saturated (Fig. 14E).

762 Following the dissolution-precipitation of chromite crystals, sulfide melt percolates  
763 downward through the nascent lower chromitite and into the porous footwall (Figs. 11 and  
764 14E; Cawthorn 1999; Naldrett *et al.* 2009; Smith *et al.* 2021). The sulfide melt may only  
765 percolate as far down as permitted by the reaction, displacing relatively buoyant evolved  
766 trapped melt upwards *en route*. This is consistent with the termination of sinuous channels  
767 comprising sulfides, silicates, and very fine-grained chromite at the base of the footwall  
768 anorthosite (Fig. 11; Smith *et al.* 2021). The upward-strengthening fabric observed in footwall  
769 cumulus plagioclase (Fig. 10) is interpreted as the result of local reordering of tabular crystals  
770 in response to the removal of intercumulus liquid (Jerram *et al.* 1996; O'Driscoll *et al.* 2010).  
771 However, trapped intercumulus melts were not fully removed from the footwall, where those  
772 trapped at the leuconorite-anorthosite transition (*i.e.*, reaction front) chemically equilibrated  
773 with relatively poikilitic orthopyroxene (Figs. 11 and 12).

774 Meanwhile, in the overlying melt, cumulus orthopyroxene and blocky chromite are  
775 accumulating above the nascent lower chromitite (Fig. 14E). The indentation of cumulus  
776 orthopyroxene causes the mm-scale undulations observed at the upper contact of the lower  
777 chromitite (ESM 3vi; Figs. 2 and 5 of Smith *et al.* 2021). A period of non-deposition must have  
778 ensued to facilitate the coarsening of this cumulus orthopyroxene by crystal aging (Fig. 14F;  
779 Cawthorn and Boerst 2006). This may have occurred when the melt that would deposit the  
780 upper chromitite replenished the chamber (Vukmanovic *et al.* 2013), supplying the heat  
781 needed to prolong the interaction between cumulus orthopyroxene, the upper portion of the  
782 lower chromitite (Fig. 7), and trapped intercumulus melt that was once part of the footwall. The

783 coarsening orthopyroxene encapsulated surrounding chromite crystals (ESM 3vi; Fig. 3C of  
784 Cawthorn and Boerst 2006) and grew downwards into the lower chromitite (Fig. 5A). It is  
785 around this time that the anorthosite “bleach zone” formed (Nicholson and Mathez 1991),  
786 whereby cumulus plagioclase beneath the lower chromitite coarsened upward into it (Fig. 5B-  
787 C; Maier and Barnes 2024). This process (described as ‘capping’ by Kerr and Tait 1986) would  
788 have discontinued chemical communication between the footwall and overlying melt, where  
789 evolved intercumulus melt would be trapped beneath this layer. This explains the relatively Ti-  
790 rich and deformed clinopyroxene oikocrysts present beneath the “bleach zone” (Fig. 5). In so-  
791 called “bleach zones”, plagioclase is strongly reversely zoned (Smith *et al.* 2021; 2023; Maier  
792 *et al.* 2021; Latypov *et al.* 2023), whereas in the lower chromitite, the ‘reverse zoning’  
793 manifests from chromite-to-chromite (*i.e.*, not rim-core-rim; Fig. 3C; Latypov *et al.* 2023). The  
794 zoning is ascribed to the preferential leaching of Na by Si-undersaturated intercumulus melts  
795 (Ballhaus and Ryan 1995; Marsh *et al.* 2021; Smith *et al.* 2023), perhaps exacerbated by the  
796 electrochemical diffusion of Na<sup>+</sup> ions into the overlying magma (Veksler *et al.* 2015).

797 A final replenishment of Cr-saturated melt occurs, which locally erodes the existing reef  
798 stratigraphy (Fig. 14G; Fig. 22 of Latypov *et al.* 2015). Blocky chromite crystals ( $\pm$  sulfide melt)  
799 are deposited at the base of the melt column and sink downwards into the coarse-grained  
800 orthopyroxene interstices (Fig. 2 of Smith *et al.* 2021). The overlying melt is saturated in sulfide  
801 melt ( $\pm$  cumulus orthopyroxene) and this melt begins to accumulate above the upper  
802 chromitite, which acted as a trap (Godel *et al.* 2006). This is consistent with relatively high  
803 proportions of sulfide melt observed in the lowermost few centimeters of the hanging-wall  
804 pyroxenite (Fig. 6B; Viljoen 1999; Smith *et al.* 2004; Beukes *et al.* 2016; Smith *et al.* 2021).

805 Sulfide melt does eventually breach the upper chromitite (Fig. 14H), displacing trapped melt  
806 upwards, consistent with the elevated bulk-rock incompatible element concentrations  
807 recorded above this sulfide-rich horizon at Rustenburg (Wilson *et al.* 1999). Moreover, the  
808 composition of chromite in the upper chromitite reflects re-equilibration with these trapped  
809 melts (Fig. 8; Barnes *et al.* 2022), which is circumstantially supported by the abundance of

810 accessory phlogopite and rutile (Figs. 6B and 7). With no further replenishment episodes, the  
811 overlying melt returns to normality, depositing undeformed cumulus orthopyroxene that  
812 records a weak lamination (Figs. 9 and 14I). Late-stage compaction was responsible for the  
813 localized misorientation observed silicate minerals (Figs. 2 and 5).

814

## 815 6. CONCLUSION

816 In the western lobe of the Bushveld Complex, the Merensky Reef is typically underlain by  
817 leuconorite and anorthosite. This study proposes that the anorthosite formed when resident  
818 leuconoritic cumulates were partially molten by an influx of relatively primitive replenishing  
819 melt. The contact between the leuconorite and anorthosite is marked by: (1) relatively  
820 increased abundance of intercumulus pyroxenes and accessory phases; (2) complex zoning  
821 profiles of cumulus plagioclase; (3) relatively low  $Mg\#_{opx}$  values, interpreted to be the result of  
822 trapped liquid shift. Although fabrics in the footwall are broadly consistent with the gravitational  
823 settling of cumulus silicates, plagioclase fabric indices strengthen with proximity to the reef.  
824 This is interpreted to result from the progressive removal of intercumulus phases and  
825 consequent reordering of cumulus plagioclase. Our data concur with previous authors  
826 suggesting that the amoeboidal chromite crystals in the lower chromitite initially formed as  
827 skeletal crystals that were subsequently reworked during an episode of dissolution-  
828 reprecipitation. The sulfide-rich sinuous networks that traverse the anorthosite formed when  
829 sulfide melt percolated into the reconstituted floor rocks. Sulfide melt percolation aided the  
830 upward displacement of trapped silicate melt, leading to the introduction of potentially volatile-  
831 and Cr-bearing silicate melts to the level of the nascent Merensky Reef. These interpretations  
832 are supported by thermodynamic models which demonstrate that replenishment-driven  
833 reconstitution of leuconoritic cumulates can trigger formation of a range of footwall lithologies,  
834 including anorthosite, norite, olivine norite, troctolite, and orthopyroxenite depending on the  
835 nature of the original floor rocks, the water content of the system, and the degree of interaction  
836 between the resident cumulates and replenishing melt.



837 **Acknowledgements**

838 Anthony Oldroyd is thanked for producing the thick sections. Hadrien Henry acknowledges  
839 CNRS funds. Stephen J. Barnes is thanked for providing insightful and constructive comments  
840 that improved the manuscript prior to submission. Zhuo-sen Yao is thanked for bringing the  
841 experimental works of R.C. Kerr and S.R. Tait to the attention of the authors. Rais Latypov,  
842 Ben Hayes, and one anonymous reviewer are thanked for their thorough and constructive  
843 reviews that helped to improve the manuscript. Christina Yan Wang is thanked for their  
844 editorial handling of this contribution.

845 **Data Availability Statement**

846 The full dataset used in this study is tabulated in the manuscript, reported in the supplementary  
847 materials, and available for free download via the CSIRO Digital Access Portal at  
848 <https://doi.org/10.25919/rgb7-ch54>.

ORIGINAL UNEDITED MANUSCRIPT

849 **References**

- 850 Arndt N, Jenner G, Ohnenstetter M, Deloule E, Wilson AH. Trace elements in the Merensky  
851 Reef and adjacent norites Bushveld complex South Africa. *Mineralium Deposita*. 2005  
852 Dec;40:550-75.
- 853 Bachmann F, Hielscher R, Schaeben H (2010) Texture analysis with MTEX–free and open-  
854 source software toolbox. In: *Solid State Phenomena*. Trans Tech Publ, pp 63–68
- 855 Baker SR, Boudreau AE (2019) The influence of the thick banded series anorthosites on the  
856 crystallization of the surrounding rock of the Stillwater Complex, Montana. *Contrib to*  
857 *Mineral Petrol* 174:1–14
- 858 Ballhaus CG (1988) Potholes of the Merensky Reef at Brakspruit Shaft, Rustenburg platinum  
859 mines; primary disturbances in the magmatic stratigraphy. *Econ Geol* 83:1140–1158
- 860 Ballhaus CG, Stumpfl EF (1986). Sulfide and platinum mineralization in the Merensky Reef:  
861 evidence from hydrous silicates and fluid inclusions. *Contributions to Mineralogy and*  
862 *Petrology*, 94(2), 193-204.
- 863 Ballhaus CG, Ryan CG (1995). Platinum-group elements in the Merensky reef. I. PGE in solid  
864 solution in base metal sulfides and the down-temperature equilibration history of  
865 Merensky ores. *Contributions to Mineralogy and Petrology*, 122, 241-251.
- 866 Barnes SJ (1986a) The effect of trapped liquid crystallization on cumulus mineral compositions  
867 in layered intrusions. *Contrib to Mineral Petrol* 93:524–531
- 868 Barnes SJ (1986b) The distribution of chromium among orthopyroxene, spinel and silicate  
869 liquid at atmospheric pressure. *Geochim Cosmochim Acta* 50:1889–1909

- 870 Barnes S-J, Maier WD (2002) Platinum-Group Element Distributions in the Rustenburg  
871 Layered Suite of the Bushveld Complex, South Africa. *Geol geochemistry Mineral Miner*  
872 *Benef Platinum-gr Elem Canad Inst Min Met Petro CIM Sp* 54:431–458
- 873 Barnes S-J, Maier WD, Curl EA (2010) Composition of the marginal rocks and sills of the  
874 Rustenburg Layered Suite, Bushveld Complex, South Africa: implications for the  
875 formation of the platinum-group element deposits. *Econ Geol* 105:1491–1511
- 876 Barnes S-J, Mansur ET, Maier WD, Prevec SA (2022) A comparison of trace element  
877 concentrations in chromite from komatiites, picrites, and layered intrusions: implications  
878 for the formation of massive chromite layers. *Can J Earth Sci* 60:97–132
- 879 Barnes SJ, Mole DR, Le Vaillant M, Campbell MJ, Verrall MR, Roberts MP, Evans NJ (2016)  
880 Poikilitic Textures, Heteradcumulates and Zoned Orthopyroxenes in the Ntaka Ultramafic  
881 Complex, Tanzania : Implications for Crystallization Mechanisms of Oikocrysts. *J Petrol*  
882 57:1171–1198.
- 883 Barnes SJ, Ryan C, Moorhead G, Latypov R, Maier WD, Yudovskaya M, Godel B, Schoneveld  
884 LE, Le Vaillant M, Pearce MB (2021) Spatial Association Between Platinum Minerals and  
885 Magmatic Sulfides Imaged with the Maia Mapper and Implications for the Origin of the  
886 Chromite-Sulfide-PGE Association. *Can Mineral*
- 887 Bohrson WA, Spera FJ, Ghiorso MS, Brown GA, Creamer JB, Mayfield A (2014)  
888 Thermodynamic model for energy-constrained open-system evolution of crustal magma  
889 bodies undergoing simultaneous recharge, assimilation and crystallization: The magma  
890 chamber simulator. *J Petrol* 55:1685–1717
- 891 Bohrson WA, Spera FJ, Heinonen JS, Brown GA, Scruggs MA, Adams JV, Takach MK, Zeff  
892 G, Suikkanen E (2020) Diagnosing open-system magmatic processes using the Magma

- 893 Chamber Simulator (MCS): part II—trace elements and isotopes. *Contrib to Mineral*  
894 *Petrol* 175:1–21
- 895 Boorman S, Boudreau A, Kruger FJ (2004) The Lower Zone–Critical Zone transition of the  
896 Bushveld Complex: a quantitative textural study. *J Petrol* 45:1209–1235
- 897 Boudreau A (1999) Fluid fluxing of cumulates: the JM reef and associated rocks of the  
898 Stillwater Complex, Montana. *J Petrol* 40:755–772
- 899 Boudreau, A. E., Mathez, E. A., & McCallum, I. S. (1986). Halogen geochemistry of the  
900 Stillwater and Bushveld Complexes: evidence for transport of the platinum-group  
901 elements by Cl-rich fluids. *Journal of Petrology*, 27(4), 967–986.
- 902 Bunge HJ (1982) *Texture analysis in materials science* Butterworths. London 11:L0
- 903 Buntin TJ, Grandstaff DE, Ulmer GC, Gold DP (1985) A pilot study of geochemical and redox  
904 relationships between potholes and adjacent normal Merensky Reef of the Bushveld  
905 Complex. *Econ Geol* 80:975–987
- 906 Cameron EN (1970) Compositions of certain coexisting phases in the eastern part of the  
907 Bushveld Complex. *Geol Soc South Africa, Spec Pap* 1:46–58
- 908 Cameron EN (1982) The upper critical zone of the eastern Bushveld Complex; precursor of  
909 the Merensky Reef. *Econ Geol* 77:1307–1327
- 910 Campbell IH (1986) A fluid dynamic model for the potholes of the Merensky Reef. *Econ Geol*  
911 81:1118–1125
- 912 Campbell IH, Murck BW (1993) Petrology of the G and H chromitite zones in the Mountain  
913 View area of the Stillwater Complex, Montana. *J Petrol* 34:291–316

- 914 Carr HW, Kruger FJ, Groves DI, Cawthorn RG (1999) The petrogenesis of Merensky Reef  
915 potholes at the Western Platinum Mine, Bushveld Complex: Sr-isotopic evidence for  
916 synmagmatic deformation. *Miner Depos* 34:335–347
- 917 Cawthorn RG (1996) Re-evaluation of magma compositions and processes in the uppermost  
918 Critical Zone of the Bushveld Complex. *Mineral Mag* 60:131–148
- 919 Cawthorn RG (1999) Permeability of the footwall cumulates to the Merensky Reef, Bushveld  
920 Complex. *South African J Geol* 102:293–310
- 921 Cawthorn RG (2002) Delayed accumulation of plagioclase in the Bushveld Complex. *Mineral*  
922 *Mag* 66:881–893
- 923 Cawthorn RG (2015) The Bushveld Complex, South Africa. In: *Layered intrusions*. Springer,  
924 pp 517–587
- 925 Cawthorn RG, Boerst K (2006) Origin of the pegmatitic pyroxenite in the Merensky unit,  
926 Bushveld Complex, South Africa. *J Petrol* 47:1509–1530
- 927 Cawthorn RG, Walraven F (1998) Emplacement and crystallization time for the Bushveld  
928 Complex. *J Petrol* 39:1669–1687
- 929 Cawthorn RG, Walsh KL (1988) The use of phosphorus contents in yielding estimates of the  
930 proportion of trapped liquid in cumulates of the Upper Zone of the Bushveld Complex.  
931 *Mineral Mag* 52:81–89
- 932 Cheadle MJ, Gee JS (2017) Quantitative textural insights into the formation of gabbro in mafic  
933 intrusions. *Elem An Int Mag Mineral Geochemistry, Petrol* 13:409–414
- 934 Eales HV, Cawthorn RG (1996) The Bushveld Complex. *Layer intrusions* 181–229

- 935 Eales HV, De Klerk WJ, Teigler B (1990) Evidence for magma mixing processes within the  
936 Critical and Lower Zones of the northwestern Bushveld Complex, South Africa. *Chem*  
937 *Geol* 88.
- 938 Eales HV, Field M, de Klerk WJ, Scoon RN (1988) Regional trends of chemical variation and  
939 thermal erosion in the Upper Critical Zone, western Bushveld Complex. *Mineral Mag*  
940 52:63–79
- 941 Eales HV, Maier WD, Teigler B (1991) Corroded plagioclase feldspar inclusions in  
942 orthopyroxene and olivine of the Lower and Critical Zones, Western Bushveld Complex.  
943 *Mineral Mag* 55:479–486
- 944 Eales HV, Marsh JS, Mitchell AA, de Klerk WJ, Kruger FJ, Field M (1986) Some geochemical  
945 constraints upon models for the crystallization of the upper critical zone-main zone  
946 interval, northwestern Bushveld complex. *Mineral Mag* 50:567–582
- 947 Eales HV, Reynolds IM (1986) Cryptic variations within chromitites of the upper critical zone,  
948 northwestern Bushveld Complex. *Econ Geol* 81:1056–1066
- 949 Ehlers TA (2005) Crustal thermal processes and the interpretation of thermochronometer  
950 data. *Rev Mineral Geochemistry* 58:315–350
- 951 Evans DM (2018) Significance of compositional zoning in cumulate chromites of the Kabanga  
952 chonoliths, Tanzania. *Mineral Mag* 82:675–696
- 953 Giorso MS, & Sack RO (1995). Chemical mass transfer in magmatic processes IV. A revised  
954 and internally consistent thermodynamic model for the interpolation and extrapolation of  
955 liquid-solid equilibria in magmatic systems at elevated temperatures and pressures.  
956 *Contrib to Mineral Petrol* 119:197–212

- 957 Godel B, Barnes S-J, & Maier WD. (2006). 3-D distribution of sulphide minerals in the  
958 Merensky Reef (Bushveld Complex, South Africa) and the JM Reef (Stillwater Complex,  
959 USA) and their relationship to microstructures using X-ray computed tomography.  
960 *Journal of petrology*, 47(9), 1853-1872.
- 961 Griffiths TA, Habler G, Ageeva O, Sutter C, Ferrière L, Abart R. (2023). The Origin of Lattice  
962 Rotation during Dendritic Crystallization of Clinopyroxene. *Journal of Petrology* 64,  
963 egac125. <https://doi.org/10.1093/petrology/egac125>
- 964 Grobler DF, Brits JAN, Maier WD, Crossingham A (2019) Litho-and chemostratigraphy of the  
965 Flatreef PGE deposit, northern Bushveld Complex. *Miner Depos* 54:3–28
- 966 Hatton CJ, Von Gruenewaldt G (1985) Chromite from the Swartkop chrome mine; an estimate  
967 of the effects of subsolidus reequilibration. *Econ Geol* 80:911–924
- 968 Hayes B, Maghdour-Mashhour R, Ashwal LD, Smith AJ, Ueckermann H, Vermeulen J. Melt  
969 infiltration in a crystal mush and pegmatoid formation in the platiniferous Merensky Reef,  
970 Bushveld Complex, South Africa. *Mineralium Deposita*. 2024 May 27:1-23.
- 971 Henry H, Kaczmarek MA, Ceuleneer G, Tilhac R, Griffin WL, O'Reilly SY, Grégoire M, Le  
972 Sueur E (2021) The microstructure of layered ultramafic cumulates: Case study of the  
973 Bear Creek intrusion, Trinity ophiolite, California, USA. *Lithos* 388–389
- 974 Henry H, Ceuleneer G, Proietti A, Kaczmarek MA, Chatelin T, de Parseval P. How does  
975 nodular chromite nucleate and grow? An integrated microstructural and petrological  
976 approach. *Journal of Petrology*. 2024 Jul;65(7):egae061.
- 977 Higgins MD (2000) Measurement of crystal size distributions. *Am Mineral* 85:1105–1116
- 978 Holwell DA, McDonald I, Butler IB (2011). Precious metal enrichment in the Platreef, Bushveld  
979 Complex, South Africa: evidence from homogenized magmatic sulfide melt inclusions.

980 Contributions to Mineralogy and Petrology, 161, 1011-1026. Holness MB (2007) Textural  
981 immaturity of cumulates as an indicator of magma chamber processes: infiltration and  
982 crystal accumulation in the Rum Eastern Layered Intrusion. J Geol Soc London 164:529–  
983 539

984 Holness MB, Vukmanovic Z, Mariani E (2017) Assessing the role of compaction in the  
985 formation of adcumulates: a microstructural perspective. J Petrol 58:643–673

986 Holtzman BK, Kohlstedt DL, Zimmerman ME, Heidelbach F, Hiraga T, Hustoft J (2003). Melt  
987 segregation and strain partitioning: Implications for seismic anisotropy and mantle flow.  
988 Science, 301(5637), 1227-1230.

989 Hulbert LJ, Von Gruenewaldt G (1985) Textural and compositional features of chromite in the  
990 lower and critical zones of the Bushveld Complex south of Potgietersrus. Econ Geol  
991 80:872–895

992 Hunt EJ, Latypov R, Horvath P (2018) The Merensky cyclic unit, Bushveld complex, South  
993 Africa: reality or myth? Minerals 8:144

994 Hunt EJ, O'Driscoll B, Day JMD (2021) Sintering as a key process in the textural evolution of  
995 chromitite seams in layered mafic-ultramafic intrusions. Can Mineral 59:1661–1692

996 Hutchinson D, Foster J, Prichard H, Gilbert S (2015). Concentration of particulate platinum-  
997 group minerals during magma emplacement; a case study from the Merensky Reef,  
998 Bushveld Complex. Journal of Petrology, 56(1), 113-159.

999 Irvine TN (1967) Chromian spinel as a petrogenetic indicator: Part 2. Petrologic applications.  
1000 Can J Earth Sci 4:71–103



- 1001 Irvine TN, Keith DW, Todd SG (1983) The JM platinum-palladium reef of the Stillwater  
1002 Complex, Montana; II, Origin by double-diffusive convective magma mixing and  
1003 implications for the Bushveld Complex. *Econ Geol* 78:1287–1334
- 1004 Janoušek V, Farrow CM, Erban V. GCDkit. Mineral: A customizable, platform-independent R-  
1005 language environment for recalculation, plotting, and classification of electron probe  
1006 microanalyses of common rock-forming minerals. *American Mineralogist*. 2024 Sep  
1007 25;109(9):1598-607.
- 1008 Jenkins MC, Mungall JE (2018) Genesis of the peridotite zone, Stillwater Complex, Montana,  
1009 USA. *J Petrol* 59:2157–2189
- 1010 Jenkins MC, Mungall JE, Zientek ML, Butak K, Corson S, Holick P, McKinley R, Lowers H  
1011 (2022) The geochemical and textural transition between the Reef Package and its  
1012 hanging wall, Stillwater Complex, Montana, USA. *J Petrol* 63:egac053
- 1013 Jenkins MC, Mungall JE, Zientek ML, Costin G, Yao ZS (2021) Origin of the JM Reef and  
1014 lower banded series, Stillwater Complex, Montana, USA. *Precambrian Res* 367:106457
- 1015 Jerram DA, Cheadle MJ, Hunter RH, Elliott MT (1996). The spatial distribution of grains and  
1016 crystals in rocks. *Contributions to Mineralogy and Petrology*, 125, 60-74.
- 1017 Kerr RC, & Tait SR (1986). Crystallization and compositional convection in a porous medium  
1018 with application to layered igneous intrusions. *Journal of Geophysical Research: Solid*  
1019 *Earth*, 91(B3), 3591-3608.
- 1020 Kinnaird JA, McDonald I (2018). The northern limb of the Bushveld Complex: a new economic  
1021 frontier. *SEG Spcl. Publ. Met. Miner. Soc.*, 21, pp. 157-177  
1022 Kruger FJ, Marsh JS (1985)  
1023 The mineralogy, petrology, and origin of the Merensky cyclic unit in the western Bushveld  
Complex. *Econ Geol* 80:958–974

- 1024 Kruger W, Latypov R (2021) Magmatic karst reveals dynamics of crystallization and  
1025 differentiation in basaltic magma chambers. *Sci Rep* 11:7341
- 1026 Langa MM, Jugo PJ, Leybourne MI, Grobler DF, Adetunji J, Skogby H. Chromite chemistry of  
1027 a massive chromitite seam in the northern limb of the Bushveld Igneous Complex, South  
1028 Africa: correlation with the UG-2 in the eastern and western limbs and evidence of  
1029 variable assimilation of footwall rocks. *Mineralium Deposita*. 2021 Jan;56:31-44.
- 1030 Latypov RM, Chistyakova S, Kaufmann FE, Roelofse F, Kruger W, Barnes SJ, Magson J,  
1031 Nicholson M (2023) The use of An-content of interstitial plagioclase for testing slurry  
1032 models for the origin of Bushveld massive chromitites. *Lithos* 460:107374
- 1033 Latypov R, Chistyakova S, Barnes SJ, Hunt EJ. (2017). Origin of platinum deposits in layered  
1034 intrusions by in situ crystallization: evidence from undercutting Merensky Reef of the  
1035 Bushveld Complex. *Journal of Petrology*. Apr 1;58(4):715-61.
- 1036 Latypov RM, Chistyakova S, Page A, Hornsey R (2015) Field evidence for the in situ  
1037 crystallization of the Merensky Reef. *J Petrol* 56:2341–2372
- 1038 Latypov RM, Chistyakova S, van der Merwe J, Westraat J (2019). A note on the erosive nature  
1039 of potholes in the Bushveld Complex. *South African Journal of Geology*, 122(4), 555-560.
- 1040 Latypov RM, Heinonen JS, Chistyakova SY (2022) Magmatic erosion of high-temperature-  
1041 melting cumulates in the Bushveld Complex by chemical dissolution. *Geosystems and*  
1042 *Geoenvironment* 1:100077
- 1043 Latypov, R., Chistyakova, S., Costin, G., Namur, O., Barnes, S., & Kruger, W. (2020).  
1044 Monomineralic anorthosites in layered intrusions are indicators of the magma chamber  
1045 replenishment by plagioclase-only-saturated melts. *Scientific Reports*, 10(1), 3839.

- 1046 Latypov RM, Namur O, Bai Y, Barnes SJ, Chistyakova S, Holness MB, Iacono-Marziano G,  
1047 Kruger WA, O'Driscoll B, Smith WD, Virtanen VJ (2024) Layered intrusions:  
1048 Fundamentals, novel observations and concepts, and controversial issues. *Earth-*  
1049 *Science Rev* 104653
- 1050 Lee CA (1983) Trace and platinum-group element geochemistry and the development of the  
1051 Merensky Unit of the Western Bushveld Complex. *Miner Depos* 18:173–190
- 1052 Leeb-Du Toit A. The Impala platinum mines. In *Mineral deposits of Southern Africa 1986* (pp.  
1053 1091-1106).
- 1054 Lee CA, Butcher AR (1990) Cyclicity in the Sr isotope stratigraphy through the Merensky and  
1055 Bastard Reef units, Atok section, eastern Bushveld Complex. *Econ Geol* 85:877–883
- 1056 Li C, Ripley EM, Sarkar A, Shin D, Maier WD (2005) Origin of phlogopite-orthopyroxene  
1057 inclusions in chromites from the Merensky Reef of the Bushveld Complex, South Africa.  
1058 *Contrib to Mineral Petrol* 150:119–130
- 1059 Maier WD (1992). Geochemical and petrological trends in the UG2 – Merensky Unit interval  
1060 of the Upper Critical Zone in the western Bushveld Complex. Unpublished Ph.D. thesis,  
1061 Rhodes University, Grahamstown, 253pp.
- 1062 Maier WD, Barnes S-J, Groves DI (2013) The Bushveld Complex, South Africa: formation of  
1063 platinum–palladium, chrome-and vanadium-rich layers via hydrodynamic sorting of a  
1064 mobilized cumulate slurry in a large, relatively slowly cooling, subsiding magma chamber.  
1065 *Miner Depos*
- 1066 Maier WD, & Barnes SJ (2024). Origin of chromitite-anorthosite interlayering in the Bushveld  
1067 Complex. *The Canadian Journal of Mineralogy and Petrology*.48:1–56

- 1068 Maier WD, Barnes SJ, Muir D, Savard D, Lahaye Y, Smith WD (2021) Formation of Bushveld  
1069 anorthosite by reactive porous flow. *Contrib to Mineral Petrol* 176:1–12
- 1070 Maier WD, Eales HV (1997) Correlation within the UG2-Merensky Reef interval of the western  
1071 Bushveld Complex, based on geochemical, mineralogical, and petrological data
- 1072 Maier WD, Halkoaho T, Huhma H, Hanski E, Barnes SJ (2018) The Penikat intrusion, Finland:  
1073 geochemistry, geochronology, and origin of platinum–palladium reefs. *J Petrol* 59:967–  
1074 1006
- 1075 Maier WD, Barnes SJ, Muir D, Savard D, Lahaye Y, Smith WD. Formation of Bushveld  
1076 anorthosite by reactive porous flow. *Contributions to Mineralogy and Petrology*. 2021  
1077 Jan;176:1-2.
- 1078 Mainprice D, Bachmann F, Hielscher R, Schaeber H (2015) Descriptive tools for the analysis  
1079 of texture projects with large datasets using MTEX: strength, symmetry and components.  
1080 *Geol Soc London, Spec Publ* 409:251–271
- 1081 Marsh BD. Crystal size distribution (CSD) in rocks and the kinetics and dynamics of  
1082 crystallization: I. Theory. *Contributions to Mineralogy and Petrology*. 1988 Jul;99:277-91.
- 1083 Marsh JS, Pasecznyk MJ, Boudreau AE (2021) Formation of chromitite seams and associated  
1084 anorthosites in layered intrusion by reactive volatile-rich fluid infiltration. *J Petrol*
- 1085 Mathez EA (1995). Magmatic metasomatism and formation of the Merensky reef, Bushveld  
1086 Complex. *Contributions to Mineralogy and Petrology*. Mar;119(2):277-86.
- 1087 Mathez EA, Hunter RH, Kinzler RJ (1997) Petrologic evolution of partially molten cumulate:  
1088 the Atok section of the Bushveld Complex. *Contrib to Mineral Petrol* 129:20–34

- 1089 Mitchell AA, Scoon RN (2007) The Merensky Reef at Winnaarshoek, Eastern Bushveld  
1090 Complex: a primary magmatic hypothesis based on a wide reef facies. *Econ Geol*  
1091 102:971–1009
- 1092 Mitchell AA, Scoon RN, Sharpe MR (2019) The Upper Critical Zone in the Swartklip Sector,  
1093 north-western Bushveld Complex, on the farm Wilgerspruit 2JQ: II. Origin by intrusion of  
1094 ultramafic sills with concomitant partial melting of host norite-anorthosite cumulates.  
1095 *South African J Geol* 2019 122:143–162
- 1096 Mudd GM, Jowitt SM, Werner TT (2018). Global platinum group element resources, reserves  
1097 and mining—A critical assessment. *Science of the Total Environment*. 1;622:614-25.
- 1098 Mungall JE, Kamo SL, McQuade S (2016) U–Pb geochronology documents out-of-sequence  
1099 emplacement of ultramafic layers in the Bushveld Igneous Complex of South Africa. *Nat*  
1100 *Commun* 7:1–13
- 1101 Naldrett AJ, Gasparri EC, Barnes SJ, Von Gruenewaldt G, Sharpe MR (1986) The Upper  
1102 Critical Zone of the Bushveld Complex and the origin of Merensky-type ores. *Econ Geol*  
1103 81:1105–1117
- 1104 Naldrett AJ, Wilson AH, Kinnaird JA, Chunnnett G (2009) PGE Tenor and Metal Ratios within  
1105 and below the Merensky Reef, Bushveld Complex: Implications for its Genesis. *Am*  
1106 *Mineral* 50:473–506
- 1107 Nicholson DM, Mathez EA (1991) Petrogenesis of the Merensky Reef in the Rustenburg  
1108 section of the Bushveld Complex. *Contrib to Mineral Petrol* 107:293–309
- 1109 O'Driscoll B, Donaldson CH, Daly JS, Emeleus CH (2009) The roles of melt infiltration and  
1110 cumulate assimilation in the formation of anorthosite and a Cr-spinel seam in the Rum  
1111 Eastern Layered Intrusion, NW Scotland. *Lithos* 111:6–20.

- 1112 O'Driscoll B, Emeleus CH, Donaldson CH, Daly JS (2010) Cr-spinel seam petrogenesis in the  
1113 Rum Layered Suite, NW Scotland: cumulate assimilation and in situ crystallization in a  
1114 deforming crystal mush. *J Petrol* 51:1171–1201
- 1115 Paton C, Hellstrom J, Paul B, Woodhead J, Hergt J. Iolite: Freeware for the visualisation and  
1116 processing of mass spectrometric data. *Journal of Analytical Atomic Spectrometry*.  
1117 2011;26(12):2508-18.
- 1118 Reid D, Basson IJ (2002) Iron-rich ultramafic pegmatite replacement bodies within the upper  
1119 critical zone, Rustenburg layered suite, Northam platinum mine, South Africa. *Mineral*  
1120 *Mag* 66:895–914
- 1121 Robb SJ, Mungall JE (2020) Testing emplacement models for the Rustenburg Layered Suite  
1122 of the Bushveld Complex with numerical heat flow models and plagioclase  
1123 geospeedometry. *Earth Planet Sci Lett* 534:116084
- 1124 Roberts MD, Reid DL, Miller JA, Basson IJ, Roberts M, Smith D (2007) The Merensky Cyclic  
1125 Unit and its impact on footwall cumulates below Normal and Regional Pothole reef types  
1126 in the Western Bushveld Complex. *Miner Depos* 42:271–292
- 1127 Sack RO (1982) Spinels as petrogenetic indicators: activity-composition relations at low  
1128 pressures. *Contrib to Mineral Petrol* 79:169–186
- 1129 Satsukawa T, Ildefonse B, Mainprice D, et al (2013) A database of plagioclase crystal  
1130 preferred orientations (CPO) and microstructures—implications for CPO origin, strength,  
1131 symmetry and seismic anisotropy in gabbroic rocks. *Solid Earth* 4:511–542
- 1132 Schannor M, Veksler IV, Hecht L, Harris C, Romer RL, Manyeruke TD (2018). Small-scale Sr  
1133 and O isotope variations through the UG2 in the eastern Bushveld Complex: The role of  
1134 crustal fluids. *Chemical Geology*, 485, 100-112.

- 1135 Schurmann LW (1993) The geochemistry and petrology of the Upper Critical Zone of the  
1136 Boshhoek section of the western Bushveld Complex. Bull van Suid-Afrika, Geol opname
- 1137 Scoates JS, Wall CJ, Friedman RM, Weis D, Mathez EA, VanTongeren JA (2021) Dating the  
1138 Bushveld Complex: Timing of Crystallization, Duration of Magmatism, and Cooling of the  
1139 World's Largest Layered Intrusion and Related Rocks. J Petrol
- 1140 Scoon RN, Costin G (2018) Chemistry, morphology and origin of magmatic-reaction chromite  
1141 stringers associated with anorthosite in the Upper Critical Zone at Winnaarshoek, Eastern  
1142 Limb of the Bushveld Complex. J Petrol 59:1551–1578
- 1143 Scoon RN, Teigler B (1995) A new LG-6 chromite reserve at Eerste Geluk in the boundary  
1144 zone between the central and southern sectors of the eastern Bushveld Complex. Econ  
1145 Geol 90:969–982
- 1146 Seabrook CL, Cawthorn RG, Kruger FJ (2005) The Merensky Reef, Bushveld Complex:  
1147 mixing of minerals not mixing of magmas. Econ Geol 100:1191–1206
- 1148 Sémoroz A, Durandet Y, Rappaz M (2001). EBSD characterization of dendrite growth  
1149 directions, texture and misorientations in hot-dipped Al–Zn–Si coatings. Acta materialia,  
1150 49(3), 529-541.
- 1151 Shaw CSJ, Dingwell DB (2008) Experimental peridotite–melt reaction at one atmosphere: a  
1152 textural and chemical study. Contrib to Mineral Petrol 155:199–214
- 1153 Skemer P, Katayama I, Jiang Z, Karato S (2005) The misorientation index: Development of a  
1154 new method for calculating the strength of lattice-preferred orientation. Tectonophysics  
1155 411:157–167

- 1156 Smith DS, Basson IJ (2006) Shape and distribution analysis of Merensky Reef potholing,  
1157 Northam Platinum Mine, Western Bushveld Complex: implications for pothole formation  
1158 and growth. *Miner Depos* 41:281–295
- 1159 Smith DS, Basson IJ, Reid DL (2004) Normal reef subfacies of the Merensky reef at Northam  
1160 platinum mine, Zwartklip facies, Western Bushveld Complex, South Africa. *Can Mineral*  
1161 42:243–260
- 1162 Smith WD, Maier WD (2021) The geotectonic setting, age and mineral deposit inventory of  
1163 global layered intrusions. *Earth-Science Rev* 220:103736
- 1164 Smith WD, Maier WD, Barnes SJ, Moorhead G, Reid D, Karykowski B (2021) Element  
1165 mapping the Merensky Reef of the Bushveld Complex. *Geosci Front* 12:101101
- 1166 Smith WD, Maier WD, Muir DD, Andersen JØ, Williams BJ, Henry H (2023) New perspectives  
1167 on the formation of the Boulder Bed of the western Bushveld Complex, South Africa.  
1168 *Miner Depos* 58:617–638
- 1169 Van der Merwe J, Cawthorn RG (2005) Structures at the base of the upper group 2 chromitite  
1170 layer, Bushveld Complex, South Africa, on Karee Mine (Lonmin Platinum). *Lithos*  
1171 83:214–228
- 1172 Veksler IV, Reid DL, Dulski P, Keiding JK, Schannor M, Hecht L, Trumbull RB (2015)  
1173 Electrochemical processes in a crystal mush: cyclic units in the Upper Critical Zone of  
1174 the Bushveld Complex, South Africa. *J Petrol* 56:1229–1250
- 1175 Vermaak CF. The Merensky Reef; thoughts on its environment and genesis (1976). *Economic*  
1176 *Geology*. 1;71(7):1270-98.
- 1177 Viljoen CF, Hieber R (1986) The Rustenburg Section of Rustenburg Platinum Mine Ltd. with  
1178 reference to the Merensky Reef. In: *Mineral Deposits of Southern Africa*. pp 1107–1134



- 1179 Viljoen MJ, Theron J, Underwood B, Walters BM, Weaver J, Peyerl W (1986). The  
1180 Amandelbult section of Rustenburg Platinum Mines Limited, with reference to the  
1181 Merensky reef. In Mineral deposits of southern Africa. pp. 1041-1060.
- 1182 Viljoen MJ (1999) The nature and origin of the Merensky Reef of the western Bushveld  
1183 Complex based on geological facies and geophysical data. South African J Geol  
1184 102:221–239
- 1185 Viljoen MJ, Theron J, Underwood B, Walters BM, Weaver J, Peyerl W (1986) The Amandelbult  
1186 section of Rustenburg Platinum Mines Limited, with reference to the Merensky reef. In:  
1187 Mineral deposits of southern Africa. pp 1041–1060
- 1188 Viring RG, Cowell MW (1999) The Merensky Reef on Northam Platinum Limited. South African  
1189 J Geol 102:192–208
- 1190 Vukmanovic Z, Barnes SJ, Reddy SM, Godel B, Fiorentini ML (2013) Morphology and  
1191 microstructure of chromite crystals in chromitites from the Merensky Reef (Bushveld  
1192 Complex, South Africa). Contrib to Mineral Petrol 165:1031–1050
- 1193 Vukmanovic Z, Holness MB, Stock MJ, Roberts RJ (2019) The creation and evolution of  
1194 crystal mush in the Upper Zone of the Rustenburg Layered Suite, Bushveld Complex,  
1195 South Africa. J Petrol 60:1523–1542
- 1196 Wager LR, Brown GM (1968) Layered igneous intrusions. Edinburgh London Oliver Boyd 1–  
1197 588
- 1198 Wagner PA (1929), The platinum deposits and mines of South Africa: Edinburgh, Oliver and  
1199 Boyd, 326 p.

- 1200 Wilson AH, Lee CA, Brown RT (1999) Geochemistry of the Merensky reef, Rustenburg  
1201 Section, Bushveld Complex: controls on the silicate framework and distribution of trace  
1202 elements. *Miner Depos* 34:657–672
- 1203 Xiong Q, Henry H, Griffin WL, Zheng JP, Satsukawa T, Pearson NJ, O'Reilly SY (2017). High-  
1204 and low-Cr chromitite and dunite in a Tibetan ophiolite: evolution from mature subduction  
1205 system to incipient forearc in the Neo-Tethyan Ocean. *Contributions to Mineralogy and  
1206 Petrology*, 172, 1-22.
- 1207 Yao Z, Mungall JE, Jenkins MC (2021) The Rustenburg Layered Suite formed as a stack of  
1208 mush with transient magma chambers. *Nat Commun* 12:505
- 1209 Yudovskaya MA, Kinnaird JA. Chromite in the Platreef (Bushveld Complex, South Africa):  
1210 occurrence and evolution of its chemical composition. *Mineralium Deposita*. 2010  
1211 Apr;45:369-91.
- 1212 Yudovskaya MA, Costin G, Shilovskikh V, Chaplygin I, McCreesh M, Kinnaird J (2019)  
1213 Bushveld symplectic and sieve-textured chromite is a result of coupled dissolution-  
1214 reprecipitation: a comparison with xenocrystic chromite reactions in arc basalt. *Contrib to  
1215 Mineral Petrol* 174:1–21
- 1216 Zaccarini F, Garuti G, Luvizotto GL, de Melo Portella Y, Singh AK. Testing trace-element  
1217 distribution and the Zr-based thermometry of accessory rutile from chromitite. *Minerals*.  
1218 2021 Jun 22;11(7):661.

Table 1. Summary of silicate mineral compositions

Phase:	Orthopyroxene												Clinopyroxene			
	leuconorite				Inor-an transition				Lower chromitite				anorthosite			
Rock type:																
Grain type:	Oikocryst				Oikocryst				Oikocryst				Oikocryst			
# Grains:	29 spots & 4 transects				5 spots & 3 transects				3 spots				5 spots			
Statistic:	<i>mi</i>	<i>ma</i>	<i>av</i>	$2\sigma$	<i>mi</i>	<i>ma</i>	<i>av</i>	$2\sigma$	<i>mi</i>	<i>ma</i>	<i>av</i>	$2\sigma$	<i>mi</i>	<i>ma</i>	<i>av</i>	$2\sigma$
	<i>n</i>	<i>x</i>	<i>e</i>		<i>n</i>	<i>x</i>	<i>e</i>		<i>n</i>	<i>x</i>	<i>e</i>		<i>n</i>	<i>x</i>	<i>e</i>	
SiO <sub>2</sub>	53.	57.	56.	2.3	53.	56.	55.	1.9	55.	57.	56.	1.0	52.	53.	53.	0.6
	2	4	3	5	2	5	4	6	4	2	5	2	7	7	3	9
	0.1	0.2	0.1	0.0	0.1	0.3	0.2	0.1	0.0	0.3	0.1	0.1	0.4	0.5	0.5	0.0
TiO <sub>2</sub>	1	8	8	9	1	6	3	8	6	5	6	6	8	6	2	7
	1.1	2.9	1.5	0.8	0.8	2.5	1.5	0.9	0.5	2.2	1.5	0.7	1.6		1.8	0.3
Al <sub>2</sub> O <sub>3</sub>	4	2	5	2	8	3	7	4	6	8	1	8	9	2.1	9	1
	0.3	0.5	0.5	0.1	0.2	0.5	0.4	0.2	0.2	0.5	0.4	0.1	0.7	0.9	0.8	0.1
Cr <sub>2</sub> O <sub>3</sub>	5	9	0	1	4	6	6	0	4	5	5	5	2	3	1	5
	12.	14.	13.	0.5	13.	16.	14.	1.7	11.	13.	12.	0.8			5.6	0.6
FeO	8	0	4	8	4	1	5	4	7	2	8	4	5.3	6.1	6	1
	0.2	0.3	0.2	0.0	0.2	0.3	0.2	0.0	0.0	0.3	0.2	0.1	0.1	0.1	0.1	0.0
MnO	1	0	6	4	4	3	7	6	9	1	4	0	3	8	6	4
	28.	29.	28.	0.5	27.	28.	28.	0.7	28.	30.	29.	1.1	16.	16.	16.	0.2
MgO	4	7	9	5	6	8	2	6	4	4	3	4	0	3	1	4
	0.9	2.0	1.6	0.6	0.9	2.3	1.5	0.7	0.3	2.1	1.3	1.2		23.	22.	0.4
CaO	2	9	6	2	9	5	2	9	6	4	1	2	22	0	8	6
	78.	80.	79.	0.7	75.	79.	77.	2.3	79.	82.	80.	1.5	82.	84.	83.	1.4
Mg#	6	0	3	7	5	2	6	2	5	3	4	4	6	5	6	3
	75.	77.	76.	0.9	74.	76.	75.	1.9	76.	79.	78.	2.3	44.	45.	45.	0.4
En	8	8	8	9	1	8	3	8	2	9	3	4	9	5	2	9
	19.	20.	20.	0.8	20.	24.	21.	2.4	17.	20.	19.	1.5	8.3	9.5	8.9	0.9
Fs	4	8	0	7	2	0	8	5	2	0	1	7	2	6	0	2
	1.7	4.0	3.1	1.2	1.9	4.5	2.9	1.5	0.7	4.0	2.5	2.2	45.	46.	45.	1.0
Wo	5	5	9	3	1	4	3	5	0	9	1	9	0	3	9	6

Phase:	Plagioclase											
	Cumulus				Cumulus				Intercumulus			
Rock type:	leuconorite				anorthosite				Lower chromitite			
Grain type:												
# Grains:	4 transects				4 transects				1 transect			
Statistic:	<i>mi</i>	<i>ma</i>	<i>av</i>	$2\sigma$	<i>mi</i>	<i>ma</i>	<i>av</i>	$2\sigma$	<i>mi</i>	<i>ma</i>	<i>av</i>	$2\sigma$
	<i>n</i>	<i>x</i>	<i>e</i>		<i>n</i>	<i>x</i>	<i>e</i>		<i>n</i>	<i>x</i>	<i>e</i>	
SiO <sub>2</sub>	45.	54.	50.	1.8	46.	66.	50.	2.1	47.	51.	50.	1.8
	1	1	0	7	7	0	5	6	0	7	5	8
	27.	32.	30.	1.4	20.	32.	30.	1.8	30.	33.	31.	1.2
Al <sub>2</sub> O <sub>3</sub>	6	0	9	3	0	2	9	2	2	4	0	6
	11.	16.	15.	1.5	2.4	16.	15.	2.1	13.	18.	15.	1.5
CaO	6	4	1	4	4	9	3	6	9	2	1	5
	1.8	4.7	2.8	0.6	2.1	10.	2.9	1.0	1.3	3.4	3.0	0.8
Na <sub>2</sub> O	9	3	1	4	9	7	1	3	9	7	4	0
	0.1	0.7	0.1	0.1	0.0	1.3	0.1	0.1	0.0	0.6	0.1	0.1
K <sub>2</sub> O	1	6	9	5	3	0	8	7	3	9	5	4
	0.1	3.1	0.3	0.8	0.0	5.1	0.4	0.8	0.1	0.6	0.2	0.1
FeO	9	7	8	0	5	9	4	5	4	5	5	7
	57.	80.	74.	5.6	11.	81.	74.	9.7	69.	87.	73.	7.0
An	5	1	8	3	9	0	3	8	4	8	2	8

<sup>1</sup>Mg# = 100 x Mg/[Mg + Fe] mol.%, En = 100 x Mg/[Mg+Fe+Ca] mol.%, Fs = 100 x Fe/[Mg+Fe+Ca] mol.%, Wo = 100 x Ca/[Mg+Fe+Ca] mol.%, An = 100 x Ca/[Ca+2Na] mol.%

**Table 2.** Compositions used for Magma Chamber Simulator modelling. Parent melt compositions are from Barnes *et al.* (2010) and footwall compositions are from Maier and Eales (1997).

<sup>1</sup> Role:	Replenishing melts		Wall rock cumulates						
Explanation:	average composition	Calculated from averages	Average UA 647.9, 649.4, and 652.9		Average IM 801, 810.1, & 818		Average IN 811.73, LK7 1389.7, EK22 272,25, & H3 1054.1		Impala 788.8
<sup>2</sup> Name:	B1	60B1:40B2	Inor	h- Inor	nor	h- nor	mnor_1	h- mnor_1	mnor_2
wt% SiO <sub>2</sub>	56.4	54.1	49.2	48.3	50.5	49.6	50.6	49.7	52.3
wt% TiO <sub>2</sub>	0.34	0.51	0.06	0.06	0.09	0.08	0.09	0.09	0.17
wt% Al <sub>2</sub> O <sub>3</sub>	12.0	13.5	28.7	28.1	22.9	22.4	19.2	18.8	12.8
wt% Fe <sub>2</sub> O <sub>3</sub>	1.36	1.42	0.05	0.05	0.09	0.09	0.18	0.18	0.69
wt% Cr <sub>2</sub> O <sub>3</sub>	0.14	0.10	0.05	0.05	0.20	0.20	0.21	0.21	0.34
wt% FeO	8.34	8.97	1.94	1.90	3.99	3.92	5.08	4.98	6.91
wt% MnO	0.18	0.19	0.02	0.02	0.02	0.02	0.10	0.10	0.17
wt% MgO	12.0	9.9	3.5	3.5	8.6	8.5	12.9	12.6	17.5
wt% NiO	0.04	0.03	0.01	0.01	0.02	0.02	0.04	0.04	0.05
wt% CaO	6.6	8.2	14.0	13.8	11.6	11.4	9.9	9.7	7.8
wt% Na <sub>2</sub> O	1.65	1.76	2.18	2.14	1.79	1.76	1.50	1.47	1.11
wt% K <sub>2</sub> O	0.99	0.69	0.18	0.17	0.08	0.08	0.05	0.05	0.04
wt% P <sub>2</sub> O <sub>5</sub>	0.08	0.11	0.02	0.02	0.01	0.01	0.04	0.04	0.01
wt% H <sub>2</sub> O	0.10	0.50	0.08	1.96	0.03	1.91	0.10	1.98	0.20
Initial T °C	1370	1285	1165	975	1195	985	1160	985	1105

<sup>1</sup>Replenishing melt compositions have been equilibrated in alphaMELTS 1.9 at their liquidus and ΔFMQ. Footwall compositions were initially equilibrated at 800°C and ΔFMQ.

<sup>2</sup>Inor = leuconorite, nor = norite, mnor = melaonrite, h- = hydrous.

1222

1223

1224

1225

1226

1227

1228

1229

1230

1231

**Table 3.** Summary of Magma Chamber Simulator outputs showing the formation of different rock types by reconstitution of floor rocks. All model outputs are available in the online repository.

Initial floor rock <sup>1</sup>	Replenishing melt (Mg#)	Initial mass of floor rock (mu)	Final floor rock temp (°C)	Relative mass of floor rock assimilated (%)	Residual floor rock	Residual floor rock assemblage (%)				Final Mg# <sup>2</sup> of Rpl melt	Replenishing melt cumulate assemblage (mu)	
						ol (Fo)	opx (Mg#)	pl (An)	Cr-spn		opx (final Mg#)	Cr-spn
Inor	60B1:40B2 (65)	10	1263	33.4	anorthosite			99.7 (82)	0.3	63.9	2.2 (85)	
Inor	60B1:40B2 (65)	20	1256	27.3	anorthosite	0.4 (90)		99.0 (81)	0.6	63.2	3.7 (85)	
Inor	60B1:40B2 (65)	30	1248	23.0	anorthosite	3.0 (89)		96.7 (81)	0.3	62.6	4.7 (84)	0.01
Inor	60B1:40B2 (65)	40	1245	21.5	anorthosite	3.4 (89)		96.3 (80)	0.3	62.1	5.8 (84)	0.03
Inor	60B1:40B2 (65)	50	1241	20.1	anorthosite	3.7 (88)		96.0 (80)	0.3	61.5	6.8 (84)	0.05
h-Inor	60B1:40B2 (65)	10	1248	42.9	anorthosite			96.4 (90)	3.6	63.4	3.2 (85)	
h-Inor	60B1:40B2 (65)	20	1213	39.6	anorthosite	0.5 (90)		95.8 (89)	3.7	62.3	5.3 (84)	0.03
h-Inor	60B1:40B2 (65)	30	1203	38.0	anorthosite	1.2 (90)		95.3 (89)	3.5	61.3	7.4 (83)	0.07
h-Inor	60B1:40B2 (65)	40	1187	36.1	anorthosite	1.9 (89)		94.8 (89)	3.3	60.3	9.1 (83)	0.10
h-Inor	60B1:40B2 (65)	50	1157	34.1	anorthosite	2.7 (88)		94.2 (88)	3.0	59.5	10.5 (82)	0.13
nor	60B1:40B2 (65)	10	1264	72.2	troctolite	11.1 (93)		84.2 (85)	4.7	63.9	3.0 (85)	
nor	60B1:40B2 (65)	20	1257	52.3	olivine norite	3.9 (91)	17.7 (90)	76.1 (83)	2.3	63.2	4.5 (85)	<0.01
nor	60B1:40B2 (65)	30	1251	38.1	norite	1.7 (88)	23.3 (89)	73.4 (81)	1.5	62.6	5.2 (84)	0.02
nor	60B1:40B2 (65)	40	1247	30.3	norite	1.1 (87)	25.2 (87)	72.4 (80)	1.2	62.0	5.9 (84)	0.03
nor	60B1:40B2 (65)	50	1244	26.5	norite	1.0 (86)	25.9 (87)	72.0 (80)	1.1	61.6	6.6 (84)	0.04
nor	B1 (70)	10	1296	82.0	anorthosite			85.2 (90)	14.8	68.7	5.5 (87)	
nor	B1 (70)	20	1279	76.2	anorthosite	4.6 (94)		84.6 (88)	10.8	67.1	9.8 (87)	
nor	B1 (70)	30	1275	69.1	troctolite	9.8 (93)		83.4 (87)	6.9	65.6	13.4 (85)	
nor	B1 (70)	40	1259	54.3	troctolite	12.8 (91)	3.4 (90)	80.7 (85)	3.0	63.9	15.6 (85)	

nor	B1 (70)	50	1245	39.9	olivine norite	8.8 (88)	12.6 (88)	76.6 (84)	2.0	62.6	16.6 (84)	
h-nor	60B1:40B2 (65)	10	1250	53.0	troctolite	20.7 (88)		74.9 (86)	4.4	63.2	3.4 (85)	
h-nor	60B1:40B2 (65)	20	1228	44.7	troctolite	22.1 (86)		75.0 (87)	2.9	62.0	5.7 (84)	0.03
h-nor	60B1:40B2 (65)	30	1197	40.0	troctolite	22.9 (85)		74.9 (87)	2.2	61.1	7.5 (83)	0.07
h-nor	60B1:40B2 (65)	40	1190	39.0	troctolite	23.0 (85)		74.9 (87)	2.1	60.1	9.4 (83)	0.11
h-nor	60B1:40B2 (65)	50	1160	36.2	troctolite	22.6 (84)	1.0 (85)	74.5 (86)	1.8	59.5	10.5 (82)	0.14
mnor	60B1:40B2 (65)	10	1261	76.9	olivine norite	36.9 (91)	20.9 (91)	36.1 (86)	6.2	63.8	3.4 (85)	
mnor	60B1:40B2 (65)	20	1254	49.6	olivine norite	12.8 (88)	34.8 (89)	50.2 (83)	2.2	62.9	4.8 (84)	0.01
mnor	60B1:40B2 (65)	30	1247	36.5	olivine norite	9.2 (87)	36.5 (88)	52.8 (82)	1.6	62.2	5.8 (84)	0.03
mnor	60B1:40B2 (65)	40	1240	28.1	olivine norite	7.8 (86)	37.0 (87)	53.9 (81)	1.3	61.7	6.5 (84)	0.04
mnor	60B1:40B2 (65)	50	1238	25.3	olivine norite	7.4 (85)	37.2 (86)	54.2 (80)	1.2	61.2	7.5 (83)	0.06
h-mnor	60B1:40B2 (65)	10	1245	57.0	troctolite	44.4 (87)		51.4 (88)	4.1	63.3	3.4 (85)	
h-mnor	60B1:40B2 (65)	20	1226	47.8	olivine norite	37.5 (86)	6.0 (87)	53.7 (88)	2.9	62.2	5.7 (84)	0.03
h-mnor	60B1:40B2 (65)	30	1209	43.1	olivine norite	34.1 (85)	9.3 (86)	54.1 (88)	2.5	61.2	7.7 (83)	0.07
h-mnor	60B1:40B2 (65)	40	1190	40.0	olivine norite	32.2 (85)	11.1 (86)	54.4 (88)	2.3	60.5	9.2 (83)	0.10
h-mnor	60B1:40B2 (65)	50	1159	37.1	olivine norite	30.8 (84)	12.4 (85)	54.7 (88)	2.1	59.8	10.6 (82)	0.14
h-mnor	B1 (70)	10	1265	78.7	troctolite	58.7 (90)		26.5 (90)	14.8	67.2	5.0 (87)	
h-mnor	B1 (70)	20	1271	75.4	troctolite	54.2 (90)		33.7 (90)	12.1	65.8	8.8 (86)	0.03
h-mnor	B1 (70)	30	1255	60.1	troctolite	45.3 (88)		49.7 (89)	5.0	64.8	10.6 (86)	0.06
h-mnor	B1 (70)	40	1228	49.4	troctolite	39.0 (86)	4.5 (87)	53.5 (88)	3.0	63.8	12.2 (85)	0.09
h-mnor	B1 (70)	50	1215	45.2	olivine norite	35.7 (86)	7.7 (86)	54.0 (88)	2.7	63.0	14.0 (84)	0.13
mnor2	60B1:40B2 (65)	10	1254	58.3	orthopyroxenite	0.4 (88)	95.4 (88)		4.2	64.9	3.4 (86)	<0.01
mnor2	60B1:40B2 (65)	20	1256	58.2	orthopyroxenite	0.1 (88)	95.6 (88)		4.3	63.6	6.4 (85)	0.05
mnor2	60B1:40B2 (65)	30	1250	50.6	orthopyroxenite		87.4 (87)	9.2 (86)	3.3	62.5	8.5 (84)	0.08
mnor2	60B1:40B2 (65)	40	1239	36.6	norite		77.3 (86)	20.4 (83)	2.2	61.7	9.4 (84)	0.10

mnor2	60B1:40B2 (65)	50	1233	31.7	norite	0.1 (86)	74.7 (86)	23.2 (82)	2.0	61.0	10.7 (84)	0.12
mnor2	B1 (70)	10	1297	61.1	orthopyroxenite	3.4 (89)	93.2 (88)		3.4	68.8	4.1 (87)	
mnor2	B1 (70)	20	1300	60.7	orthopyroxenite	3.0 (89)	93.5 (88)		3.5	67.3	7.5 (87)	
mnor2	B1 (70)	30	1300	60.6	orthopyroxenite	2.9 (89)	93.6 (88)		3.5	65.9	10.7 (86)	
mnor2	B1 (70)	40	1281	59.6	orthopyroxenite	1.8 (89)	94.4 (88)		3.8	64.7	13.3 (85)	
mnor2	B1 (70)	50	1256	58.2	orthopyroxenite		95.7 (88)		4.3	63.8	15.5 (85)	

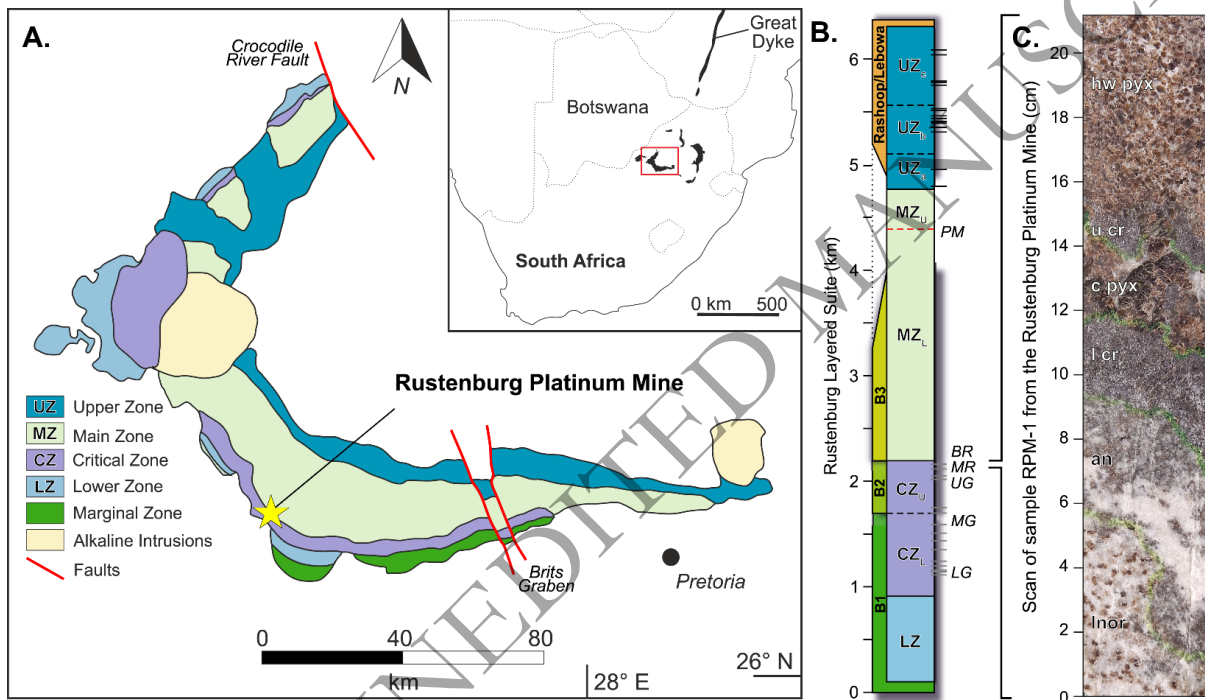
<sup>1</sup>Inor = leuconorite, nor = norite, mnor = melanorite, h- = hydrous.

1232

ORIGINAL UNEDITED MANUSCRIPT

1233 **Figures**

1234 **Figure 1.** Geological map (A) and schematic stratigraphic section (B) of the Bushveld Complex  
 1235 showing the location of the Rustenburg Platinum Mine in the western lobe (modified from  
 1236 Mungall *et al.* 2016). **C.** Annotated photograph of sample RPM-1 described in detail by Smith  
 1237 *et al.* (2021). Abbreviations: Inor = leuconorite, an = anorthosite, l cr = lower chromitite, c pyx  
 1238 = central pyroxenite, u cr = upper chromitite, hw pyx = hanging-wall pyroxenite.

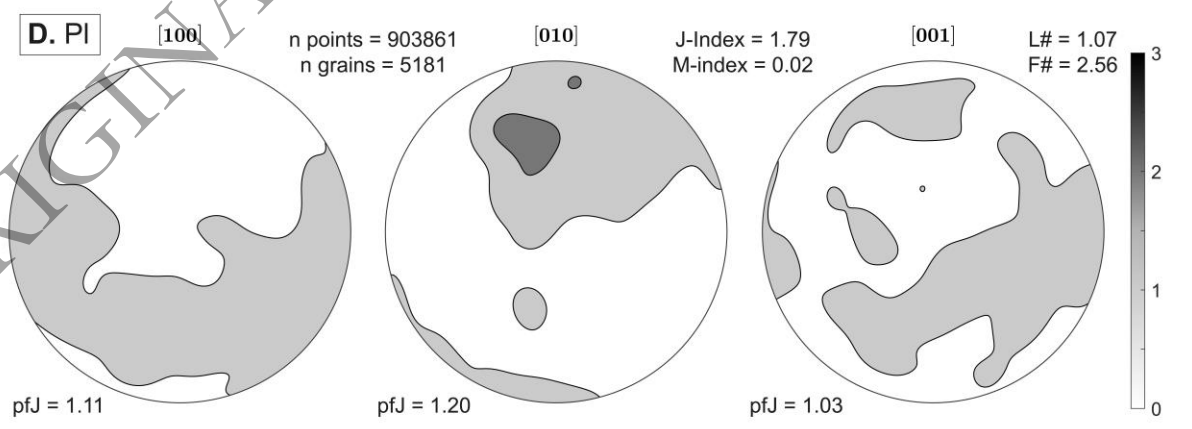
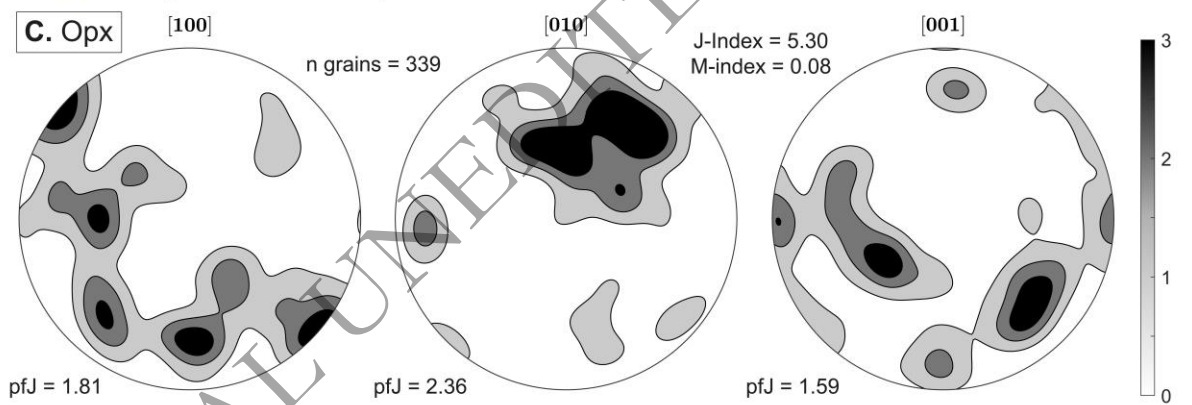
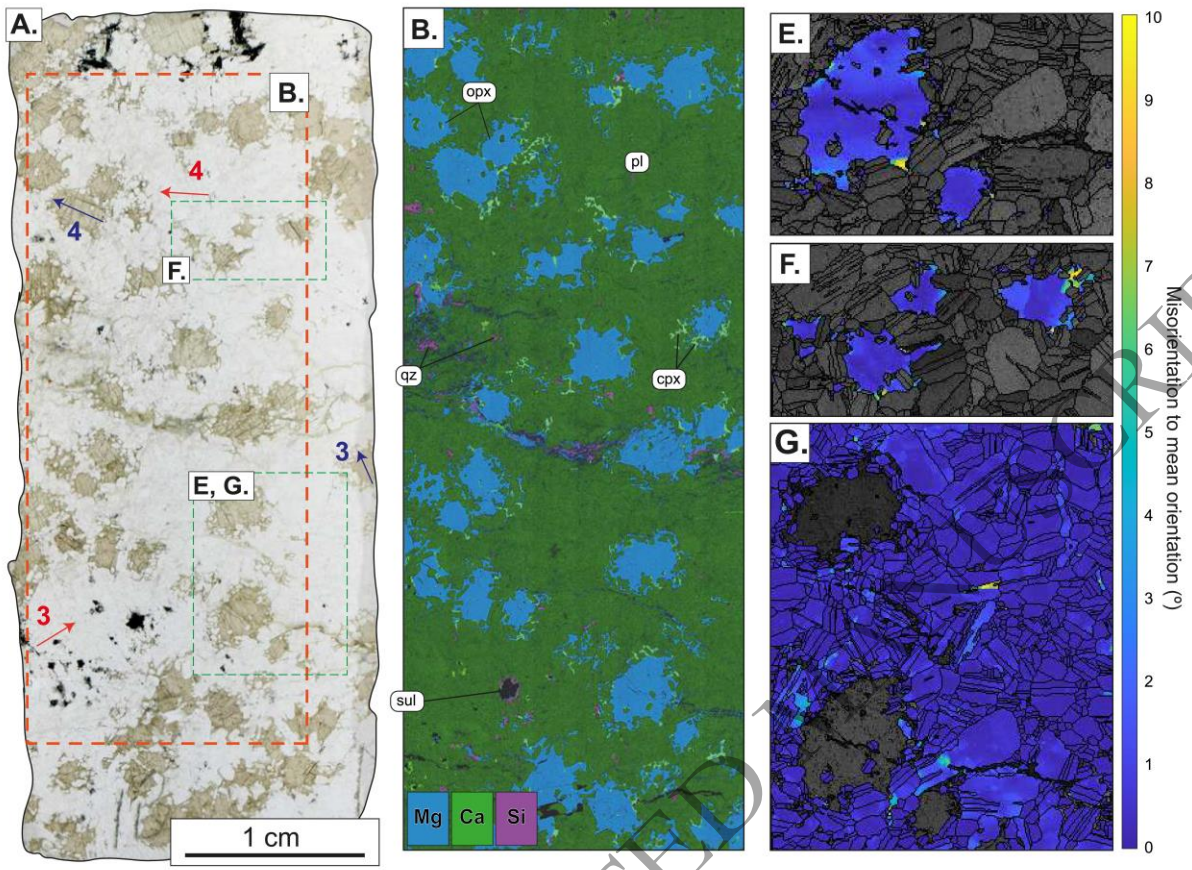


1239  
 1240  
 1241  
 1242  
 1243  
 1244  
 1245  
 1246  
 1247



1248 **Figure 2.** Summary of map data acquired for the leuconorite. **A.** Scanned image of section B1  
1249 showing analyzed areas and locations of EPMA profiles in orthopyroxene (blue arrows) and  
1250 plagioclase (red arrows). **B.** Mg-Ca-Si element map displaying cumulus plagioclase (pl),  
1251 orthopyroxene (opx) with intercumulus outer margins, as well as traces of intercumulus  
1252 clinopyroxene (cpx) and quartz (qz). **C.** Lower hemisphere, equal-area pole figures of the  
1253 [100], [010], and [001] axes of orthopyroxene crystals (one point per crystal). **D.** Lower  
1254 hemisphere, equal-area pole figures of the [100], [010], and [001] axes of all measurements  
1255 from plagioclase crystals. **E-F.** Map of misorientation-to-mean orientation of orthopyroxene  
1256 crystals. Note the small amounts of misorientation confined to the rims. **G.** Map of  
1257 misorientation-to-mean orientation of cumulus plagioclase crystals showing minimal evidence  
1258 of deformation.

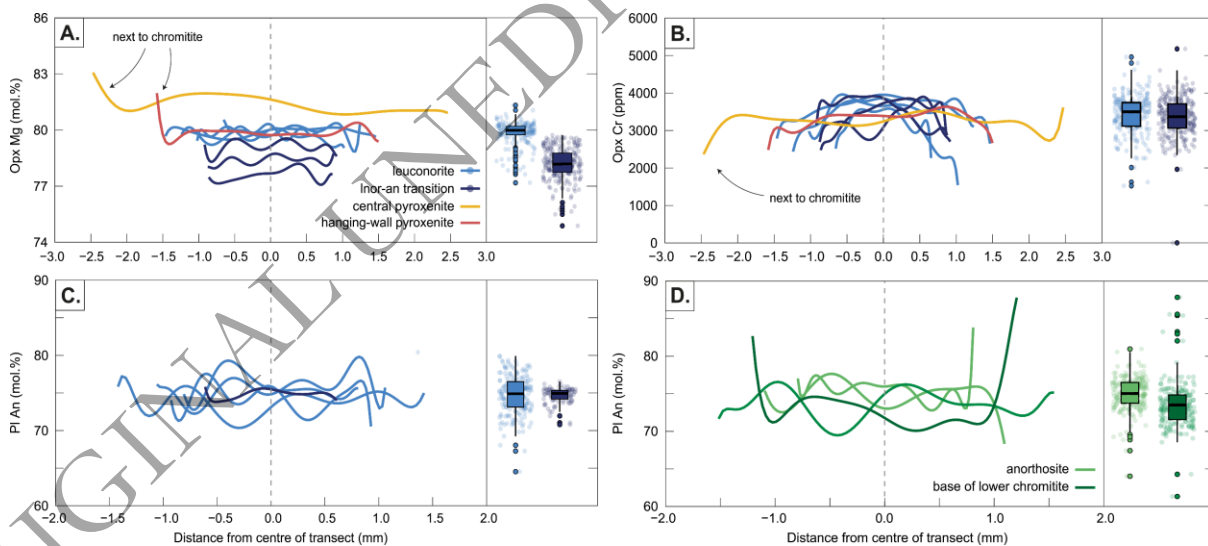
ORIGINAL UNEDITED MANUSCRIPT



1259

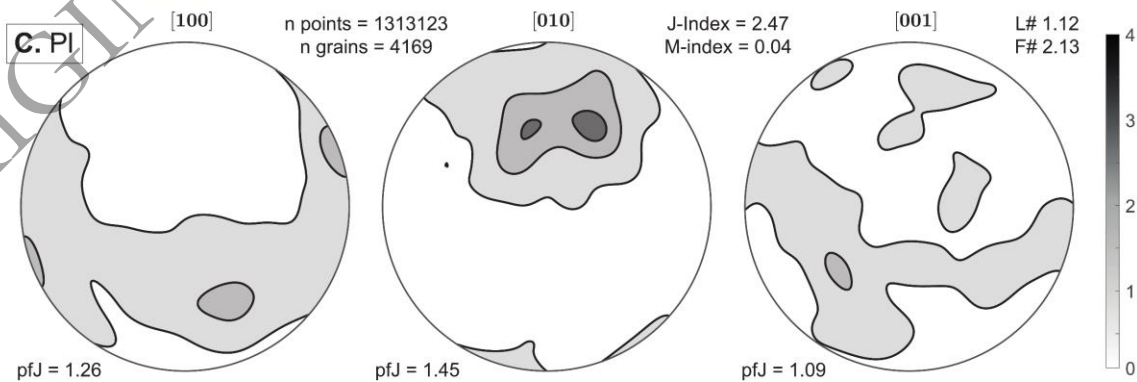
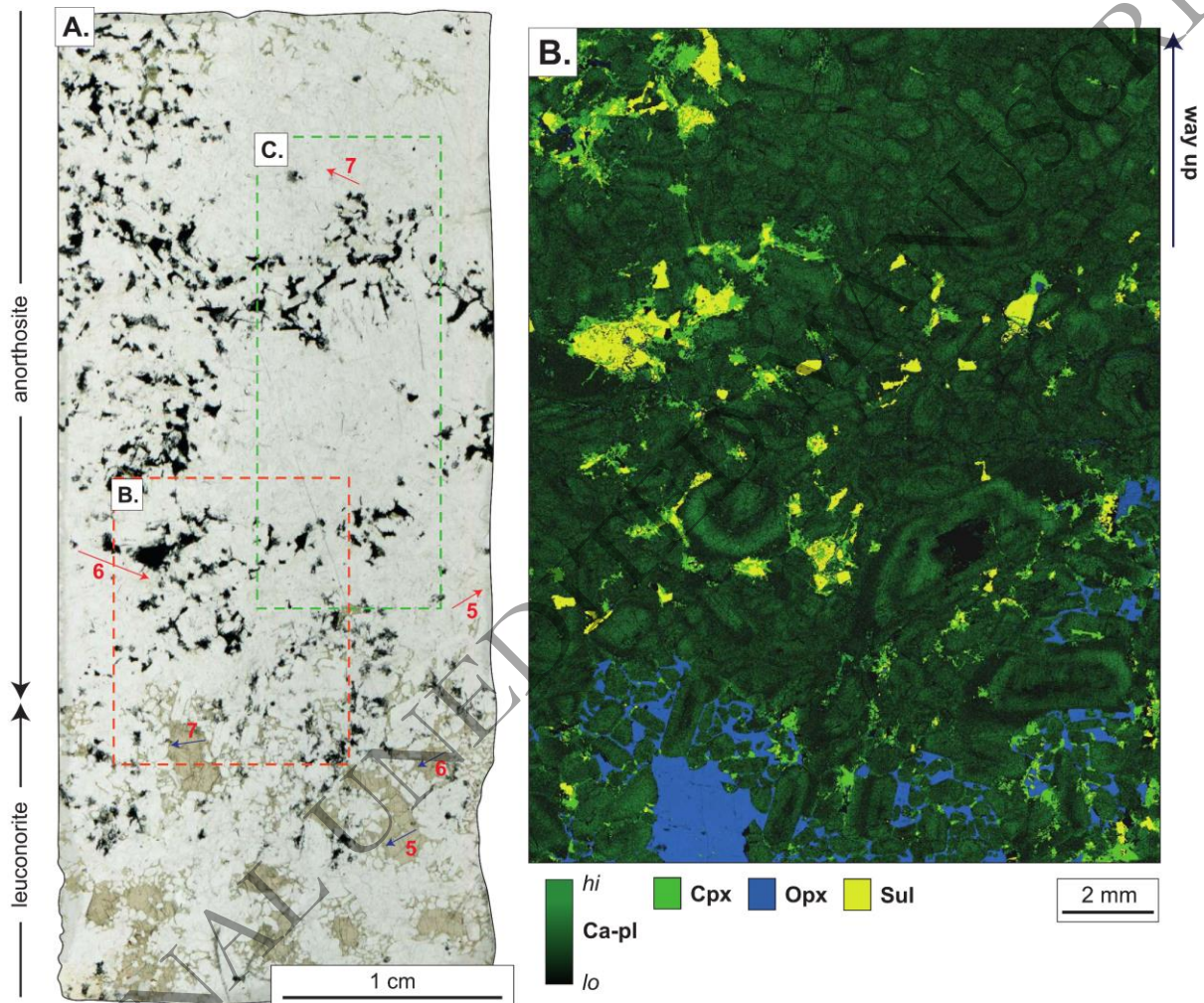
1260

1261 **Figure 3. A-B.** Rim-core-rim transects of Mg# (mol.%) and Cr (ppm) contents of  
 1262 orthopyroxene crystals analyzed in the leuconorite together with an orthopyroxene crystal  
 1263 analyzed in the central and hanging-wall pyroxenites (blue transects 8 and 9 in Fig. 6).  
 1264 Orthopyroxene crystals at the leuconorite-anorthosite (Inor-an) transition have lower Mg#  
 1265 values and similar Cr concentrations compared with those from the underlying leuconorite.  
 1266 The Mg# values are broadly flat, whereas Cr concentrations decrease towards crystal rims.  
 1267 Note that the orthopyroxene crystal from the central pyroxenite has higher Mg# values, which  
 1268 increase with proximity to chromite crystals. **C-D.** Transects of An contents for plagioclase  
 1269 crystals in the footwall anorthosite and at the base of the lower chromitite. Plagioclase crystals  
 1270 show no discernible systematic zoning. The crystal analyzed in the lower chromitite shows  
 1271 pronounced reverse zoning, though this does not represent rim-core-rim but a portion of a  
 1272 plagioclase oikocryst that occupies the space between two chromite crystals (red transect 9  
 1273 in Fig. 6). Box-and-whisker diagrams with jittered data points are included and the lines  
 1274 represent polynomial approximations.



1275  
 1276  
 1277  
 1278  
 1279

1280 **Figure 4.** Summary of map data acquired for the lower portion of the footwall anorthosite. **A.**  
 1281 Scanned image of section C1 showing the analyzed areas (blue arrows for orthopyroxene,  
 1282 red arrows for plagioclase). **B.** Ca-Na element map highlighting complex plagioclase zoning  
 1283 at the leuconorite-anorthosite contact. **C.** Lower hemisphere, equal-area pole figures of the  
 1284 [100], [010], and [001] axes of all measurements taken on plagioclase crystals.

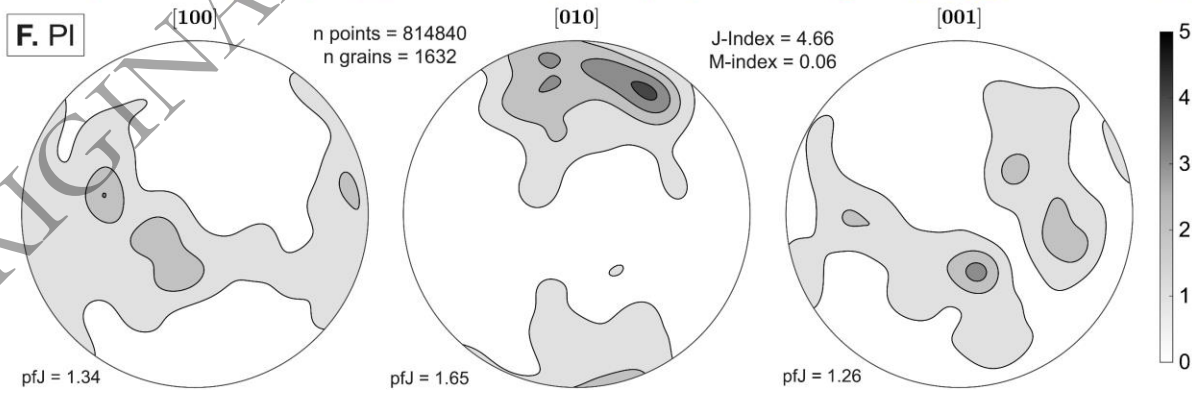
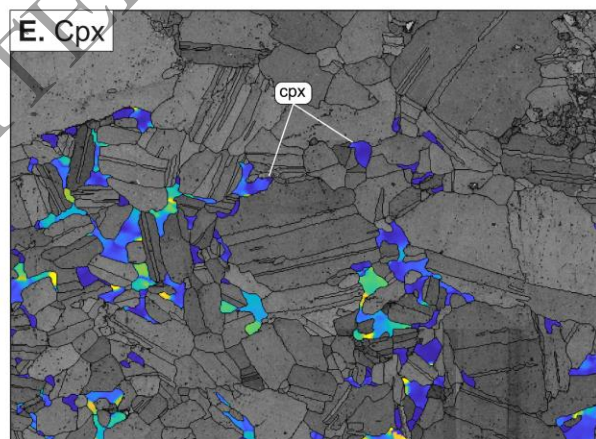
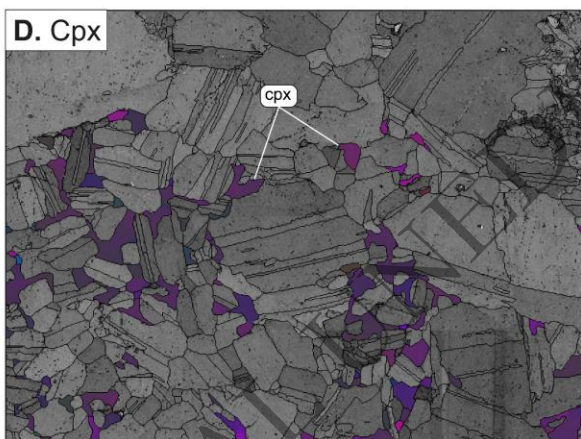
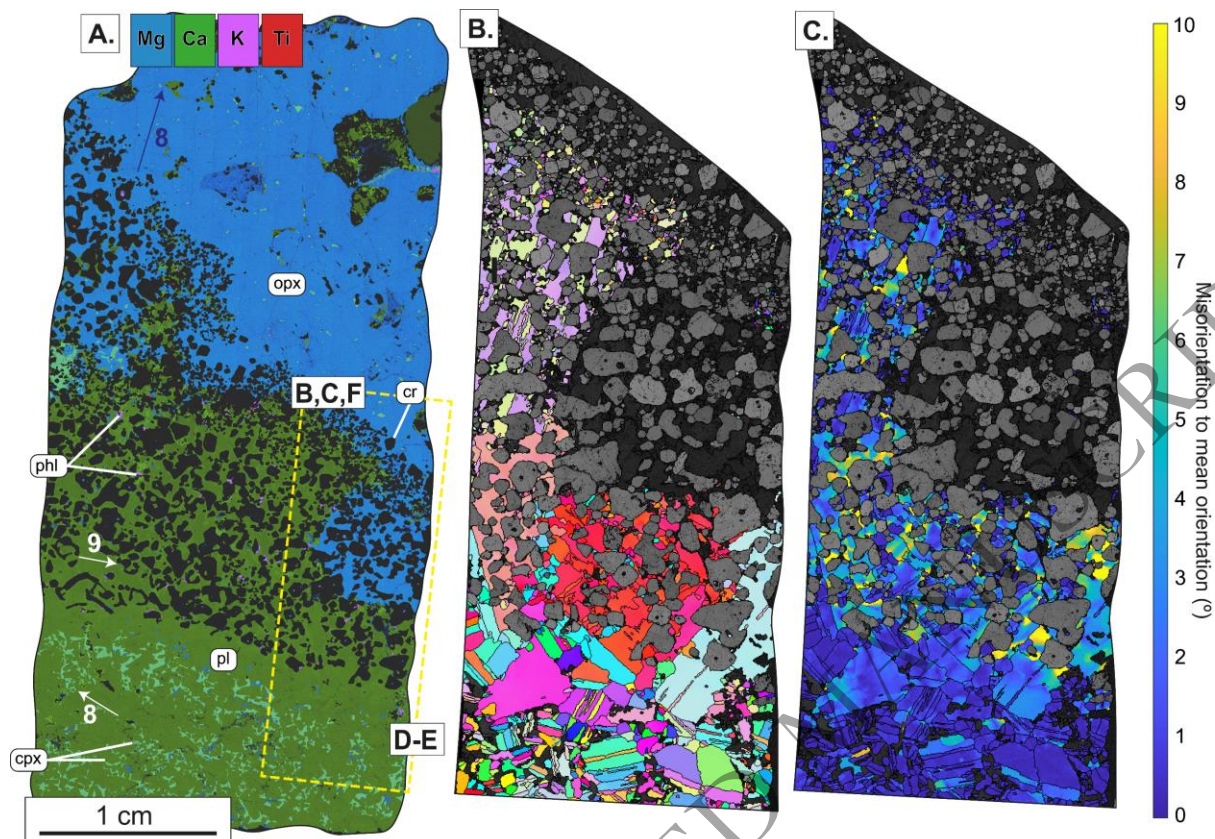


1285

1286

1287 **Figure 5.** Summary of data acquired for the upper portion of the footwall anorthosite. **A.** Mg-  
1288 Ca-Si element map of section D1 displaying textures at the anorthosite-lower chromitite-  
1289 central pyroxenite interval. Note that the upper portion of the anorthosite is essentially  
1290 leucogabbro with the exception of a nearly pure layer of anorthosite directly beneath the lower  
1291 chromitite. **B-C.** Mean orientation (similar colors mean similar orientations) and misorientation-  
1292 to-mean orientation maps of plagioclase. Note the large plagioclase oikocrysts are orientated  
1293 with their (010) planes normal to the layering plane and display large degrees of localized  
1294 misorientation. **D-E.** Mean orientation and misorientation-to-mean orientation maps of a  
1295 clinopyroxene oikocryst in the anorthosite beneath the lower chromitite. **F.** Lower hemisphere,  
1296 equal-area pole figures of the [100], [010], and [001] axes of all measurements taken on  
1297 plagioclase crystals.

ORIGINAL UNEDITED MANUSCRIPT



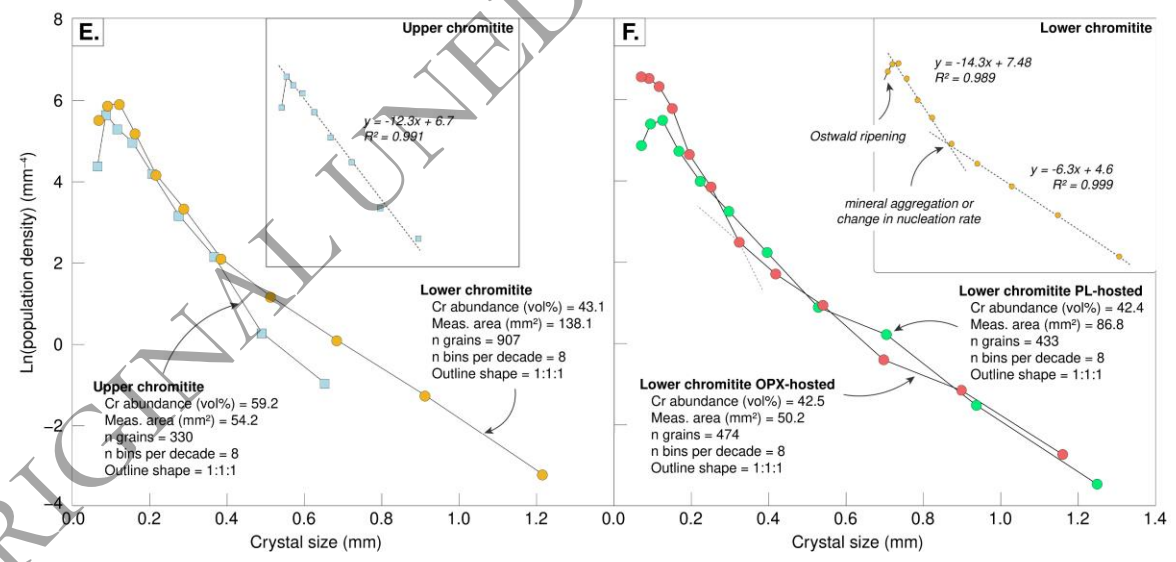
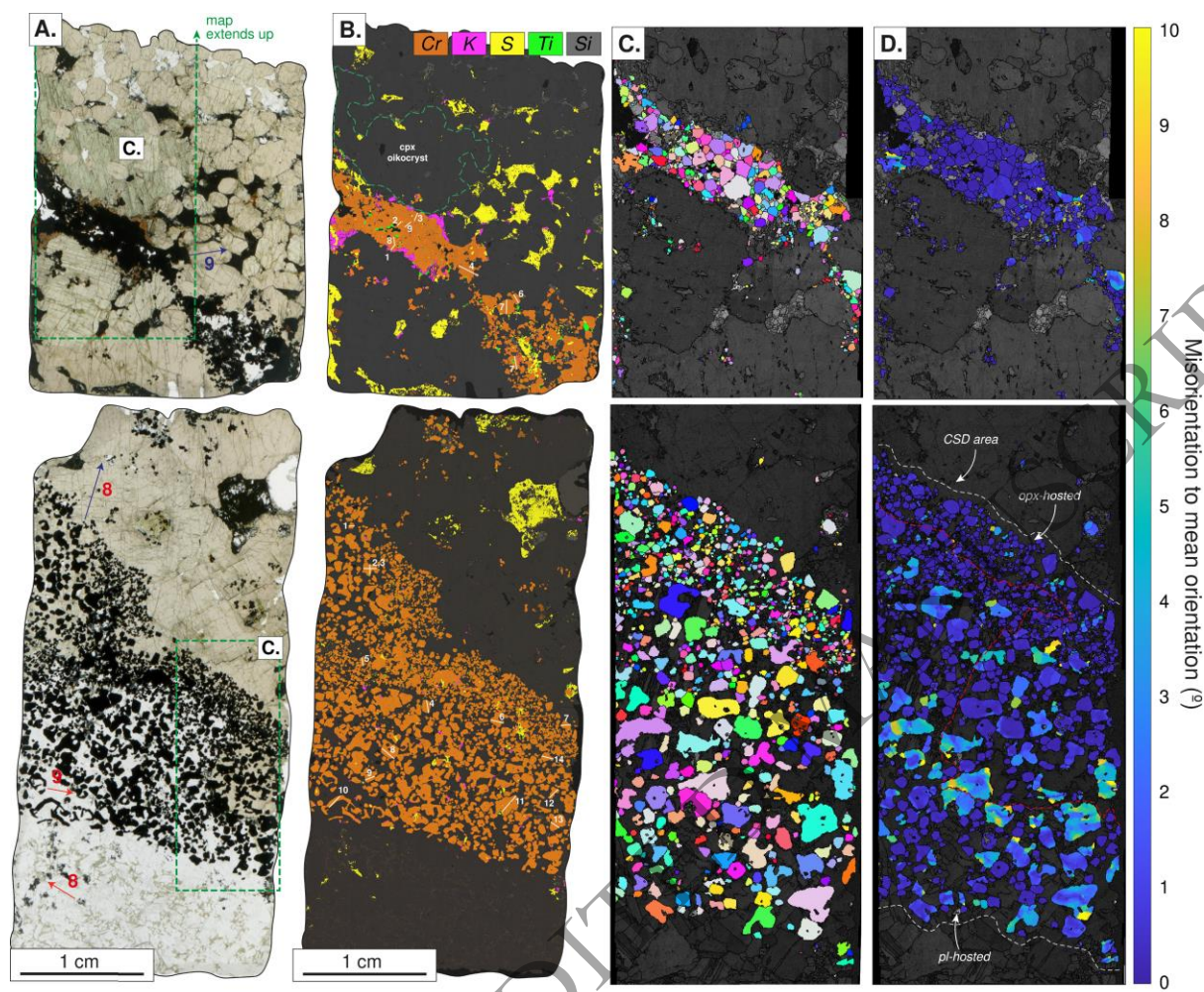
1298

1299

1300

1301 **Figure 6.** Microtextural data acquired for the lower and upper chromitites. **A.** Plane-polarized  
1302 light scans of sections D1 and E1, showing the locations of analyses. **B.** Cr-K-S-Ti-Si element  
1303 map highlighting the distribution of sulfides, rutile, and phlogopite (white lines are chromite LA-  
1304 ICP-MS transects). **C-D.** Mean orientation and misorientation-to mean orientation maps of  
1305 chromite. Note the seemingly random distribution of chromite grains, which themselves occur  
1306 as either: (i) relatively coarse and amoeboidal crystals with large degrees of misorientation;  
1307 (ii) relatively fine and blocky crystals with no internal misorientation. **E-F.** Crystal size  
1308 distribution curves for chromite crystals. Each profile displays concave patterns at crystal sizes  
1309 < 0.2 mm and shallow convex patterns at crystal sizes > 2 mm. Note the 'kink' at ~ 0.34 mm  
1310 in the profiles of orthopyroxene-hosted crystals in the lower chromitite.

ORIGINAL UNEDITED MANUSCRIPT



1311

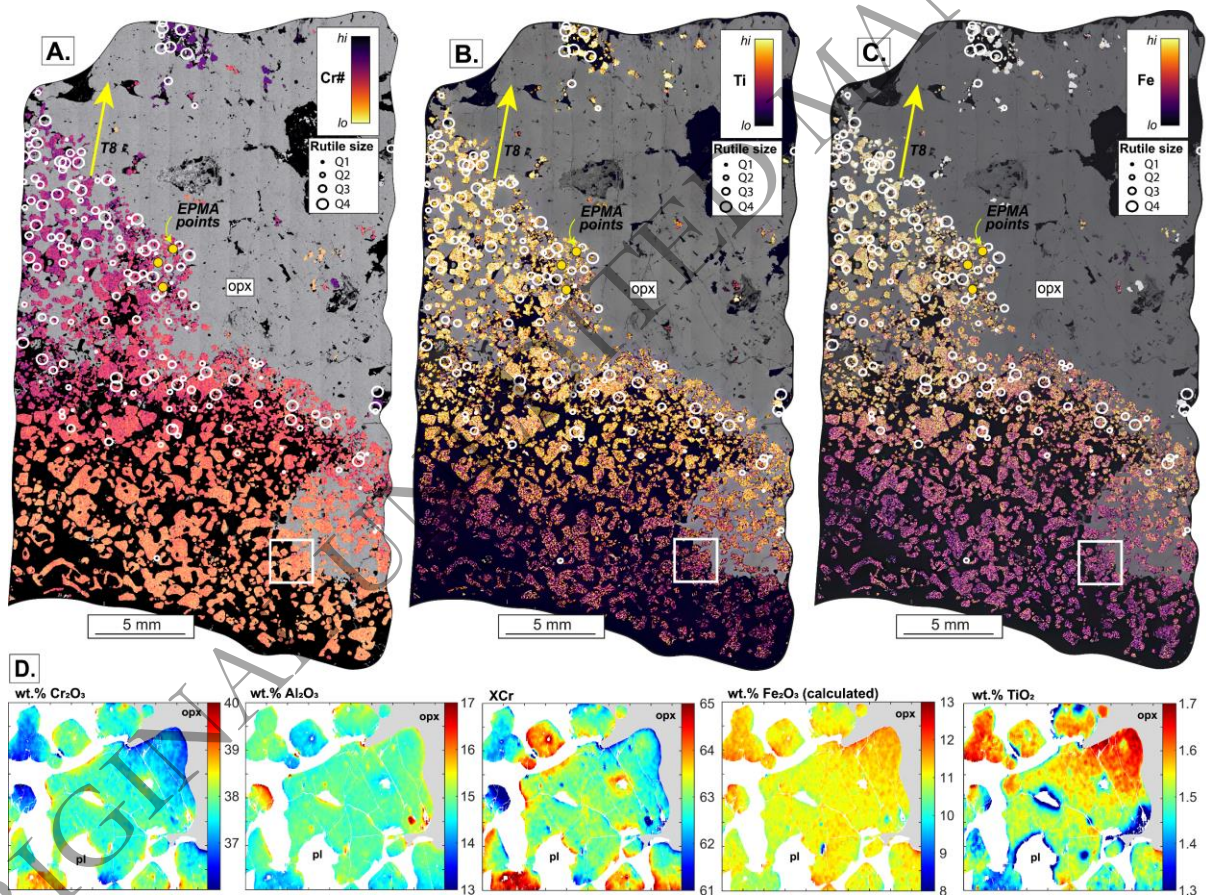
1312

1313

1314

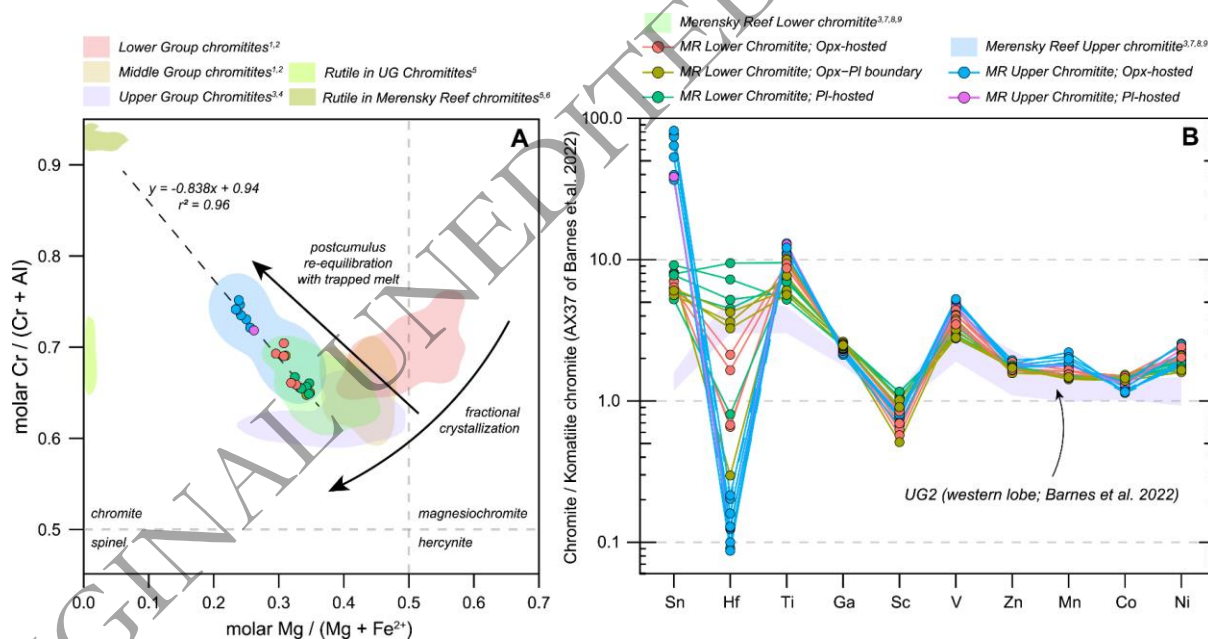


1315 **Figure 7.** Chemical maps of chromite crystals in the lower chromitite. **A-C.** Semi-quantitative  
 1316 EDS maps of Cr# values, Ti concentrations, and Fe concentrations. The grey phase is is  
 1317 orthopyroxene (opx) and all other phases are in black. White circles indicate rutile and yellow  
 1318 annotations are the locations of EPMA analyses. Note that chromite crystals in the upper  
 1319 portion of the lower chromitite are relatively Al-poor, Ti-rich, and Fe-rich, and also coincide  
 1320 with the appearance of accessory rutile. **D.** EPMA map of chromite crystals occurring at the  
 1321 contact between plagioclase and orthopyroxene oikocrysts. Although there appears to be  
 1322 compositional change with proximity to orthopyroxene, this pattern does not extend to all  
 1323 orthopyroxene-hosted crystals.



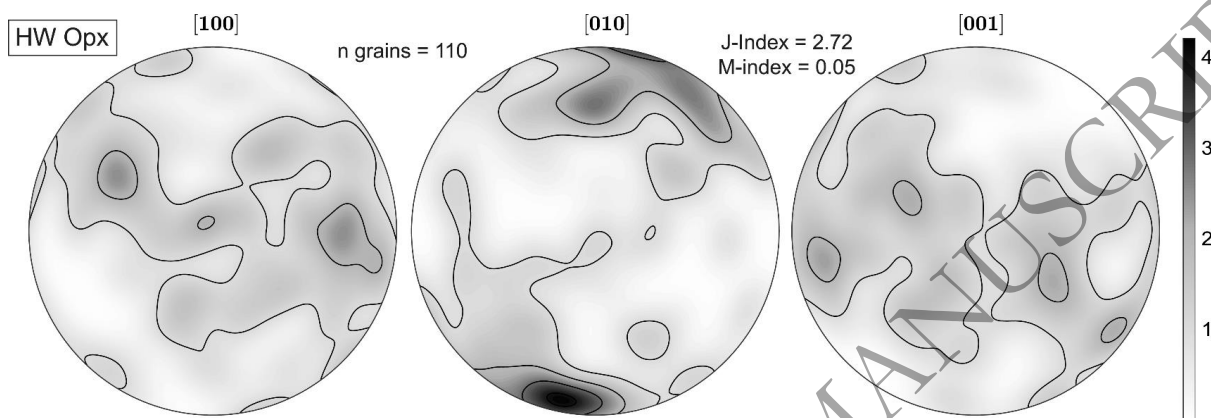
1324  
 1325  
 1326  
 1327

1328 **Figure 8. A.** Molar Mg# values *versus* Cr# values for chromite crystals. Upper chromitite  
 1329 crystals have relatively lower Mg# and higher Cr# values compared with lower chromitite  
 1330 crystals. This pattern is consistent with those determined from other studies on the Merensky  
 1331 chromitites and can be explained through postcumulus reaction with residual trapped liquids  
 1332 (Barnes *et al.* 2022). Conversely, massive chromitites in the Critical Zone display trends that  
 1333 are overall more consistent with that expected of fractional crystallization (Yudovskaya and  
 1334 Kinnaird 2010). Rutile compositions from the UG and Merensky chromitites are underlain,  
 1335 where Merensky rutile has relatively high Cr# values. **B.** Chromite trace element  
 1336 concentrations normalized to komatiite chromite AX37 of Barnes *et al.* (2022) underlain by the  
 1337 field of UG2 chromite in the western lobe (Barnes *et al.* 2022). <sup>1</sup>Hatton and von Gruenewaldt  
 1338 (1985), <sup>2</sup>Naldrett *et al.* (2009), <sup>3</sup>Barnes *et al.* (2022), <sup>4</sup>Langa *et al.* (2021), <sup>5</sup>Zaccarini *et al.*  
 1339 (2021), <sup>6</sup>Scoon and Costin (2018), <sup>7</sup>this study, <sup>8</sup>S-J. Barnes unpub, <sup>9</sup>Vukmanovic *et al.* (2013).



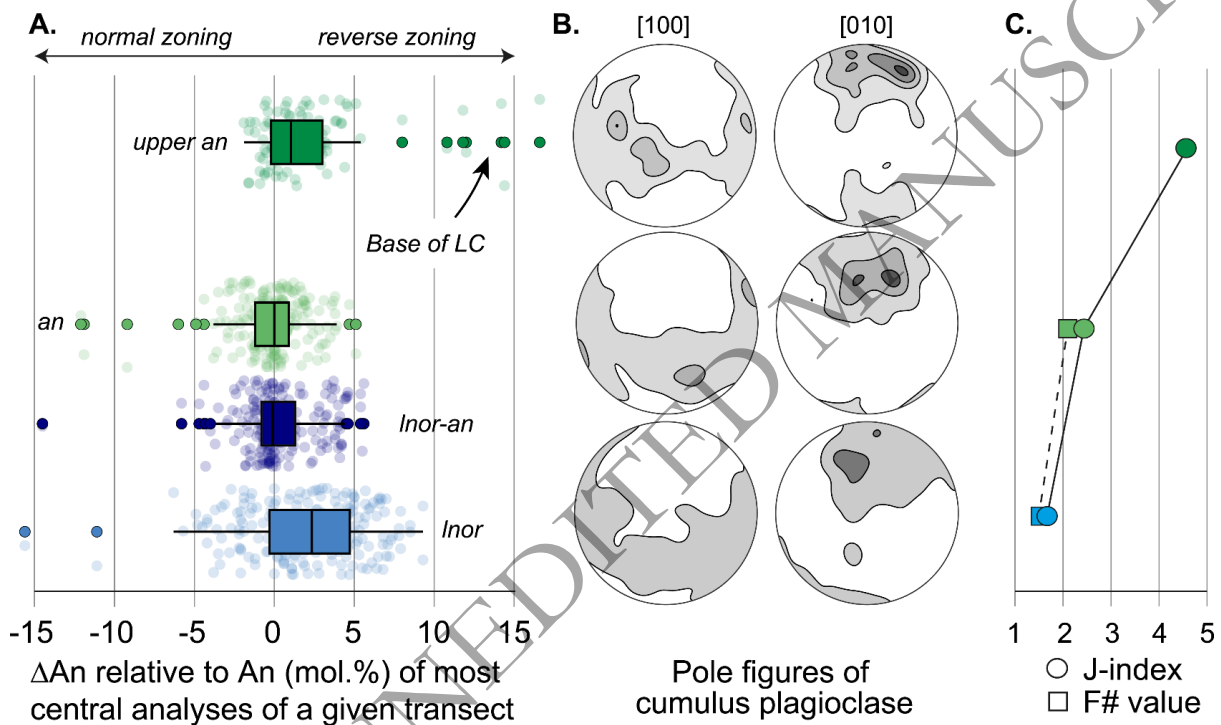
1340  
 1341  
 1342  
 1343  
 1344

1345 **Figure 9.** Lower hemisphere, equal-area pole figures of the [100], [010], and [001] axes of  
1346 orthopyroxene crystals (one point per crystal) from the lowermost hanging-wall pyroxenite.  
1347 Note that the hanging-wall cumulates record a weak planar fabric similar to those of the  
1348 footwall leuconorite.



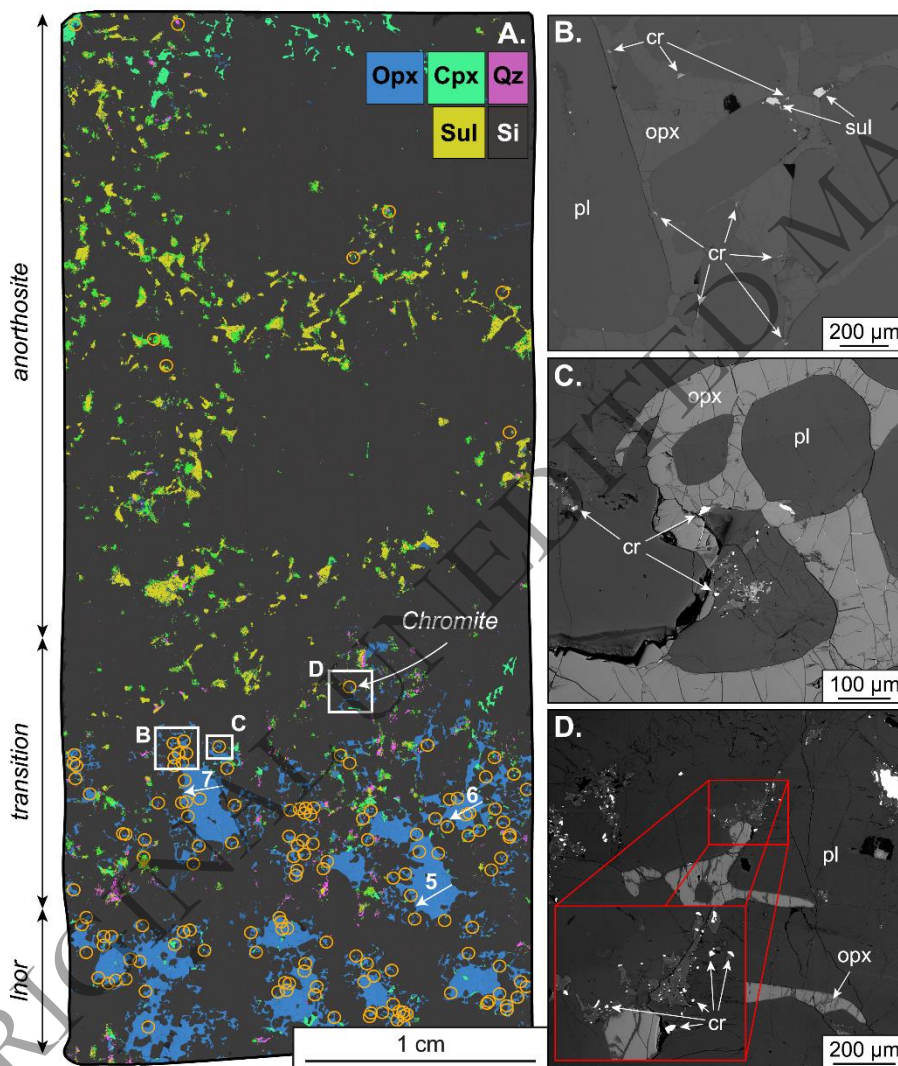
1349  
1350  
1351  
1352  
1353  
1354  
1355  
1356  
1357  
1358  
1359  
1360  
1361  
1362

1363 **Figure 10.** Plagioclase compositions and microtextures in the Merensky Reef footwall. **A.** Box-  
 1364 and-whisker diagrams of  $\Delta An$  content relative to the An content of the most central analytical  
 1365 point of a given transect. Note the anomalous reverse zoning of plagioclase in the upper  
 1366 anorthosite (*i.e.*, directly beneath the lower chromitite). **B.** [100] and [010] pole figures of  
 1367 cumulus plagioclase. **C.** J-index and F# values of cumulus plagioclase throughout the footwall.  
 1368 Note that the strength of the CPO increases with proximity to the reef.



1369  
 1370  
 1371  
 1372  
 1373  
 1374  
 1375  
 1376  
 1377

1378 **Figure 11.** Nature of chromite (cr) crystals in the Merensky footwall. **A.** Si-Mg-Ca-S element  
 1379 map of section C1, which intersects the leuconorite-anorthosite transition. Note the more  
 1380 poikilitic nature of orthopyroxene, relative increase in intercumulus clinopyroxene, quartz (qz),  
 1381 and sulfide (sul) at the transition, as well as the distribution of very fine-grained chromite  
 1382 (circled by orange rings). Arrows correspond to EPMA transects. **B-D.** Backscattered electron  
 1383 images of very fine-grained chromite at the margins of orthopyroxene (opx) oikocrysts in the  
 1384 transition zone.



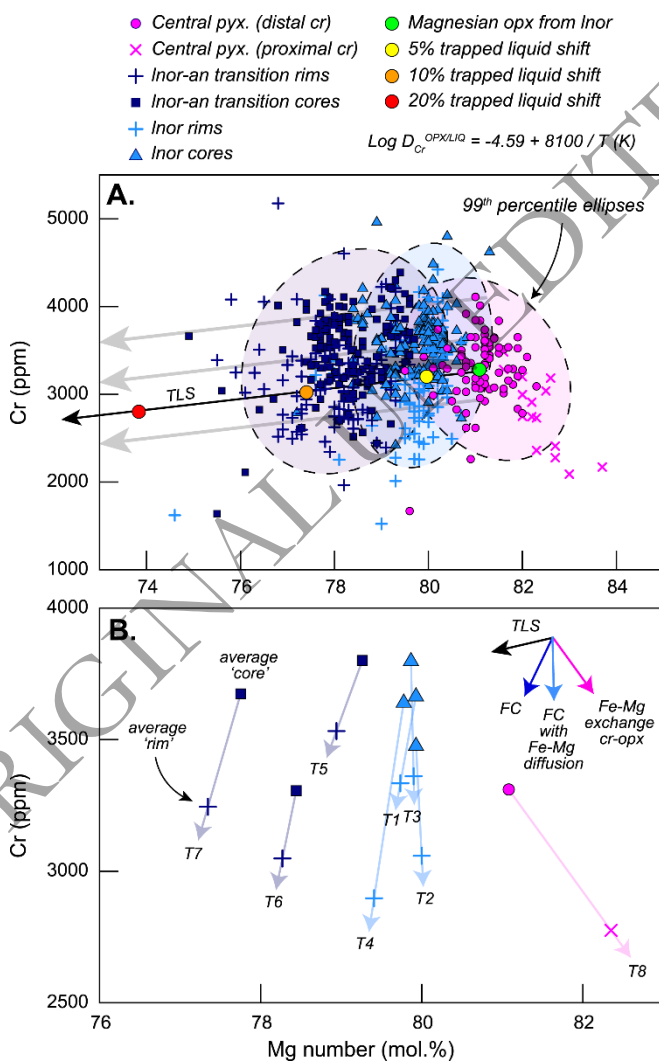
1385

1386

1387

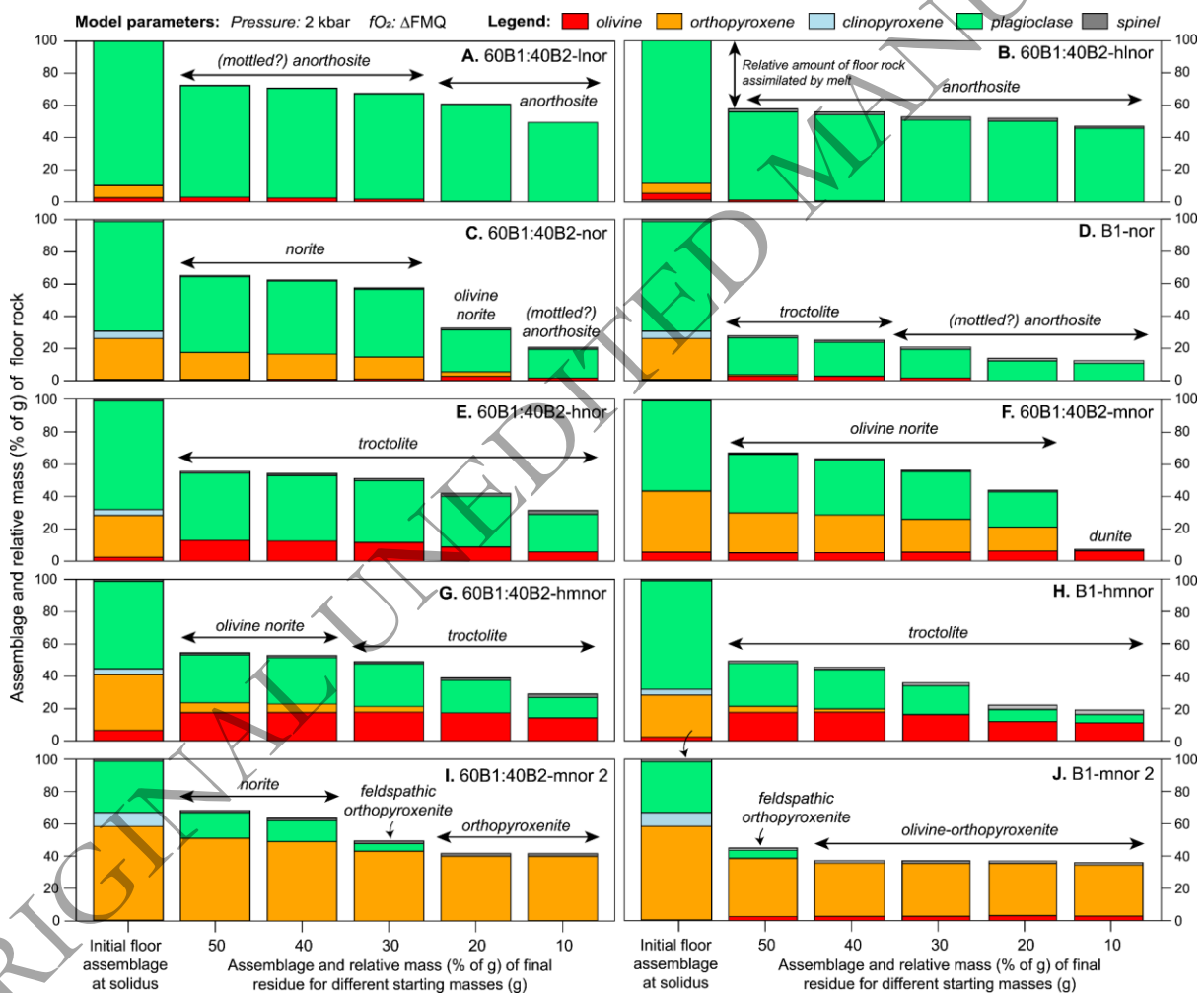
1388

1389 **Figure 12.** Composition of orthopyroxene and nature of the leuconorite-anorthosite (Inor-an)  
 1390 transition. **A.** Orthopyroxene core and rim compositions from the footwall and central  
 1391 pyroxenite (pyx) underlain by 99<sup>th</sup> percentile ellipses. The colored circles and arrows highlight  
 1392 the compositional effect of trapped liquid shift (TLS), whereby the Mg# values of poikilitic  
 1393 orthopyroxene at the leuconorite-anorthosite transition may have been lowered during  
 1394 interaction with up to 10% trapped interstitial liquid. **B.** Average core and rim compositions for  
 1395 individual orthopyroxene crystals analyzed in the footwall lithologies and central pyroxenite.  
 1396 Rim compositions were averaged from the outermost 20% analytical points. The compositions  
 1397 of orthopyroxene crystals in the footwall are consistent with variable degrees of fractional  
 1398 crystallization (FC), Fe-Mg diffusion, and TLS, whereas orthopyroxene in the central  
 1399 pyroxenite has undergone chemical exchange with chromite.



1400

1401 **Figure 13.** Results from Magma Chamber Simulator models (also summarized in Table 3).  
 1402 The diagrams show the final mass (relative to the initial starting mass that has been  
 1403 normalized to 100) and assemblage of the floor rocks following the interaction with  
 1404 replenishing 60B1:40B2 or B1 melt. The illustrated floor rocks include leuconorite (A-B), norite  
 1405 (C-E), melanorite (F-H), and high-Mg melanorite (I-J). Note that this interaction is capable of  
 1406 reconstituting resident noritic cumulates to a restite of anorthosite, norite, troctolite, olivine  
 1407 norite, or orthopyroxenite under different initial conditions. All models are available at  
 1408 doi.org/10.25919/rgb7-ch54.

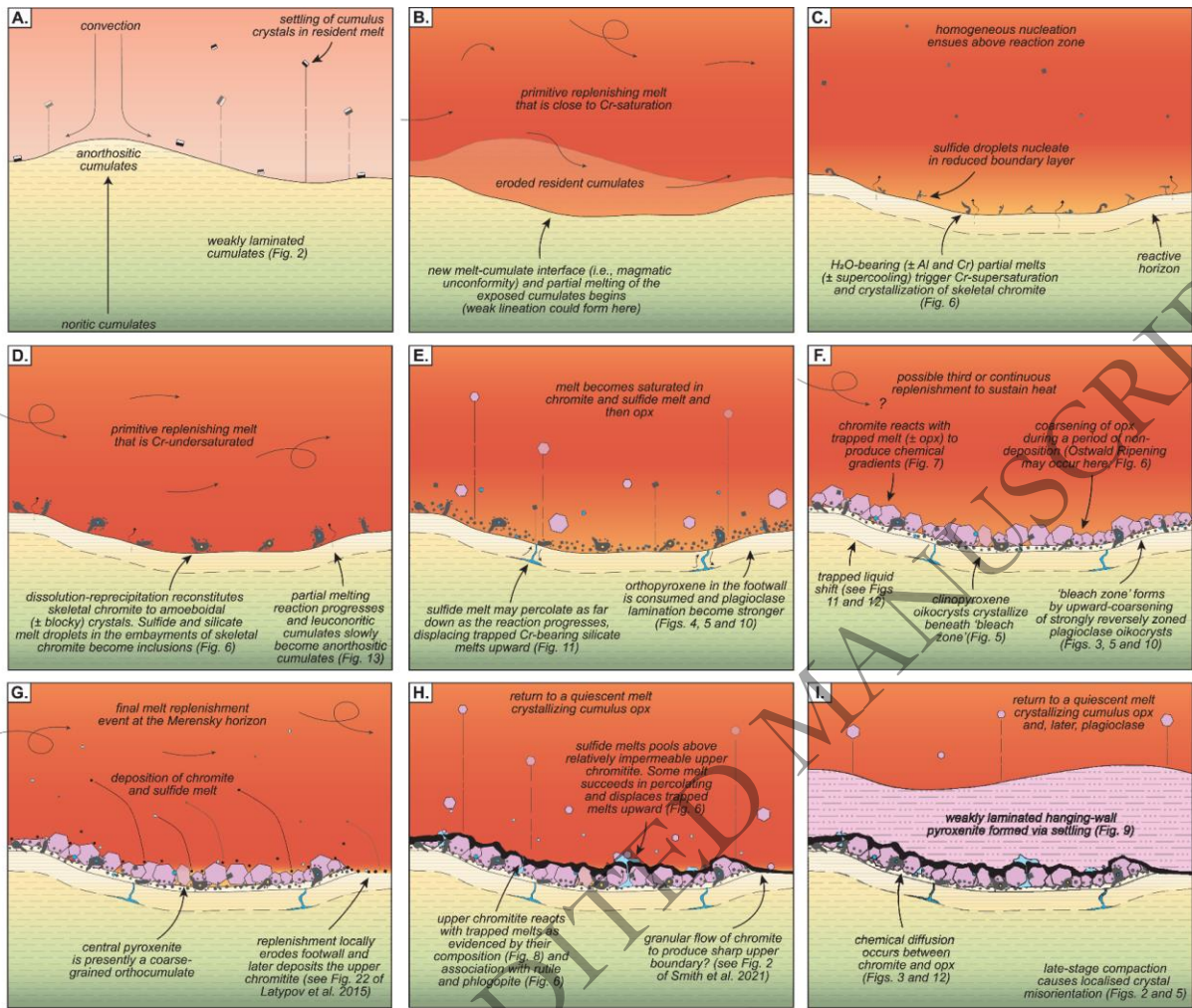


1409  
 1410  
 1411  
 1412

1413 **Figure 14.** Schematic model for the formation of the Merensky Reef (Rustenburg facies) and  
1414 its footwall anorthosite. Full details are outlined in *Section 5.7*. **A.** Deposition of leuconoritic  
1415 cumulates by gravitational settling of cumulus silicates in a quiescent melt. **B-C.** Basal  
1416 influx(es) of relatively primitive melt that erodes and partially melts the resident leuconoritic  
1417 cumulates. Skeletal chromite ( $\pm$  sulfide melt) crystallizes during this reaction. **D-E.**  
1418 Replenishment by Cr-undersaturated melt triggers dissolution-reprecipitation of skeletal  
1419 chromite. This melt later deposits chromite, sulfide melt, and then orthopyroxene, where the  
1420 sulfide melt percolates down into the now-porous footwall cumulates. Partial melting and the  
1421 resulting modification of the mineral composition of the residue in the footwall continues. **F.**  
1422 Cumulus orthopyroxene and plagioclase coarsen during an episode of non-deposition and  
1423 sustained heat brought about by continuous (or subsequent) replenishment. **G.** A final episode  
1424 of melt replenishment locally erodes the footwall cumulates and deposits the upper chromitite  
1425 ( $\pm$  sulfide melt). **H-I.** Sulfide melt and then cumulus orthopyroxene settle above the upper  
1426 chromitite, forming the hanging-wall pyroxenite, where some sulfide melt percolates  
1427 downward into the orthocumulate central pyroxenite.

ORIGINAL UNEDITED MANUSCRIPT





1428  
 1429  
 1430  
 1431  
 1432  
 1433  
 1434  
 1435  
 1436  
 1437  
 1438  
 1439

1440 **Supplementary Material**

1441 **Electronic Supplementary Material 1.** Supplementary Methods.

1442 **Electronic Supplementary Material 2.** A series of supplementary tables reporting: (1) EPMA  
1443 mineral compositions; (2) Physical properties and compositions of chromite crystals; (3) MCS  
1444 modelling summary.

1445 **Electronic Supplementary Material 3.** Electronic Supplementary Figures 3i to 3vi.

1446 **Online Supplementary Repository.** doi.org/10.25919/rgb7-ch54. Contains: (1) Source  
1447 reports for EPMA analytical sessions; (2) Raw EBSD files and MTEX outputs; (3) Original  
1448 CSDcorrections files for Crystal Size Distributions; (4) Original EPMA map outputs; (5) Raw  
1449 MCS models.

1450

ORIGINAL UNEDITED MANUSCRIPT



# Deltech Furnaces

Sustained operating  
temperatures to 1800°  
Celsius

[www.deltechfurnaces.com](http://www.deltechfurnaces.com)



Gas Mixing System



An ISO 9001:2015 certified company

Custom Vertical Tube



ASME NQA-1 2008 Nuclear Quality Assurance

Standard Vertical Tube



Control systems are certified by Intertek UL508A compliant

Bottom Loading Vertical Tube